Sensors & Actuators: B. Chemical 410 (2024) 135717

Contents lists available at ScienceDirect

Sensors and Actuators: B. Chemical

journal homepage: www.elsevier.com/locate/snb

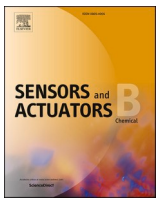

Microfluidic integration of μPID on μcolumn for ultracompact micro-gas chromatography

Xiaheng Huang [a,b,c,d,1], Shuo Yang [a,c,d,1], Wencheng Li [a,b,c,d], Robert Nidetz [e], Ruchi Sharma [a,c,d], Anjali Devi Sivakumar [a,b,c,d], Chandrakalavathi Thota [a,c,d], Hongbo Zhu [a], Weishu Wu [a,c,d], Seong-Yong Jeong [a,c,d], Xudong Fan [a,c,d,*]

[a] Department of Biomedical Engineering, University of Michigan, Ann Arbor, MI 48109, USA
[b] Department of Electrical Engineering and Computer Science, University of Michigan, Ann Arbor, MI 48109, USA
[c] Center for Wireless Integrated MicroSensing and Systems (WIMS^2), University of Michigan, Ann Arbor, MI 48109, USA
[d] Max Harry Weil Institute for Critical Care Research and Innovation, University of Michigan, Ann Arbor, MI 48109, USA
[e] Lurie Nanofabrication Facility, University of Michigan, Ann Arbor, MI 48109, USA

ARTICLE INFO

Keywords:
Gas Chromatography
Gas Sensing
Microfabrication
Photo-ionization detector
GC column

ABSTRACT

Microfabricated gas chromatography (μGC) offers a powerful portable vapor analysis solution for various field applications. Here, we developed a microfluidically integrated architecture of a microfluidic photoionization detector (μPID) on a microfabricated column (μcolumn) via a silicon-on-insulator platform. By eliminating the off-chip interconnects, the microfluidically integrated column PID (iCPID) demonstrated a narrow peak width compared to the off-chip benchmark μPID. Furthermore, the iCPID sensitivity as a function of the bias voltage and temperature were characterized. Finally, an ultracompact (0.9 L, 0.9 kg), automated, and battery-operated μGC system without any benchtop components was constructed based on the iCPID. Rapid (2 min) isothermal separation of eight volatile compounds at room temperature was demonstrated.

1. Introduction

Lab-on-a-chip microfabricated gas chromatography (μGC) [1] has revolutionized the analysis of volatile organic compounds (VOCs) by enabling compact, low-power, and rapid analysis in diverse field applications, including environmental monitoring [2–5], biomedical diagnosis [6–8], homeland security [9–12] and space exploration [13,14]. To date, the majority of μGC devices rely on a hybrid integration approach [1–5,10,12,15–25], in which individual components (*i.e.*, preconcentrators, columns, and detectors, *etc.*) are fluidically connected using off-chip interconnects (*e.g.*, guard columns and universal connectors, *etc.*). Although this approach offers advantages such as eliminating thermal crosstalk between components that usually operate at different temperatures and providing greater freedom to optimize and change individual components, it also poses several challenges. First, manual assembly of a hybrid integrated μGC is labor-intensive, costly, and susceptible to human errors, making it incompatible with mass production. Second, fluidic interfacing methods [26] commonly used in hybrid integration (*e.g.*, epoxy, Nanoport [27], metal fittings [12,28,29], and manifolds [3,4,12,25,30], *etc.*) can either introduce mechanically weak points at the connecting junctions or significantly increase the footprint of presumably miniaturized components. Finally, the hybrid configuration can generate cold spots and dead volumes between transfer lines, thereby causing band broadening and degrading overall chromatographic separation ability of μGC. Consequently, monolithically integrated μGC has been pursued, with a focus on integrating separation micro-columns (μcolumns) and respective detectors on a single chip [11,30–36]. Table 1 compares recent μGC systems and modules employing different integration schemes. Compared to hybrid integration, monolithic integration could range from only merging two devices (or partial components) together to an entire system level integration of multiple devices on the same chip. It is widely observed that integration in μGC systems often includes additional packaging post-fabrication for inevitable off-chip interconnections (fluidics, ionization sources, *etc.*).

Various types of gas detectors, including thermal conductivity

* Corresponding author at: Department of Biomedical Engineering, University of Michigan, Ann Arbor, MI 48109, USA.
E-mail address: xsfan@umich.edu (X. Fan).
[1] Equal contribution

https://doi.org/10.1016/j.snb.2024.135717
Received 23 January 2024; Received in revised form 12 March 2024; Accepted 26 March 2024
Available online 30 March 2024

detectors (TCD) [11,34,35], optical interferometric sensors [31], pivot plate resonators [30], photoionization detectors (PID) [32,33] have been integrated monolithically with μcolumns owing to their microfabrication compatibility. Among these integrated detectors, PIDs have emerged superior due to their fast response, high sensitivity, and ability to detect a broad range of chemical compounds. Recently, μGC integrated with a micro helium discharge photoionization detector (μDPID) showed rapid separation and detection of alkanes and aromatics with a detection limit of 10 pg [32,33]. However, the μDPID requires a separate high-purity helium cartridge as an auxiliary flow during operation, which inevitably increases the footprint and weight of the entire system, and requires constant maintenance for cartridge replacement, thus restricting certain field applications. In contrast, vacuum ultraviolet (VUV) lamp based PIDs avoid the need for bulky helium cartridges and can potentially be integrated with μGC. Although the lower VUV photon energies generated from the VUV lamp (10.6 eV for Kryton lamps and 11.7 eV for Argon lamps) may limit the range of detectable chemical compounds, they allow for the use of ambient air (after removal of hydrocarbons and drying) as the carrier gas without interfering with analysis of target compounds since oxygen and nitrogen ionization potentials are higher than 11.7 eV. This further reduces the μGC system's footprint by eliminating any carrier gas cartridges. Finally, the plasma in lamp-based PIDs is confined inside the lamp and not in direct contact with the electrodes (as in the case of μDPID [39,40]), which prevents the potential degradation of the electrodes (both excitation and sensing electrodes) exposed to plasma over time.

Conventional PIDs using VUV lamps are still relatively bulky, and their configuration is not designed for μGC integration. Zhu et al. and Li et al. developed a lamp-based microfluidic PID (μPID) with rapid response and high sensitivity. This μPID was fabricated on a silicon wafer using etched parallel silicon channel walls as the electrodes on a glass substrate [18,41], paving a way for potential μGC integration. Very recently, a lamp-based PID (arrayed integrated photoionization detector, AiPD) using coplanar metal sensing electrodes has also been explored in an attempt for integration with μcolumns [16]. In the μDPID-μcolumn work [32,33], the microfabrication process for monolithically integrating the μDPID and μcolumn, although relatively simple (*i.e.*, a two-mask process), was yet not amicable for wafer-scale batch production due to the need for dicing the silicon and glass wafers into separate individual pieces before anodic bonding (in order to expose the excitation/sensing electrodes for packaging) and the simplified process disallowed an on-chip heater [34] conventionally integrated on μcolumns [32,33]. Similarly, the AiPD-μcolumn device [16] currently was only realized by manually gluing individually microfabricated dies on a larger substrate using epoxy, which may hinder large-scale manufacturing [16]. Furthermore, coplanar metal electrode design as in both μDPID and AiPD [16,32,33], while relatively simple to fabricate, would result in non-uniform electric fields that may lead to a sublinear response to analyte concentrations [16]. On the other hand, for the μPID using parallel silicon electrodes that generate a strong and uniform electric field [18,41] overlapping entirely with the photoionization area, its integration requires an appropriate design that can achieve fluidic connection between the μPID and μcolumn while maintaining electrical isolation.

Here, we developed an integrated μGC architecture based on a silicon-on-insulator (SOI) structure that enables monolithic integration of the parallel-plate silicon electrodes on μcolumn with an on-chip heater, realizing microfluidic integration of a VUV lamp based μPID with additional microfluidic packaging (*i.e.*, VUV lamp, fused silica capillaries) off-chip. In this article, we first detail the design, fabrication, and characterization of the integrated μcolumn and μPID (*i.e.*, iCPID). It is shown that at lower injection masses (<10 ng), the iCPID maintained a sensitivity similar to the stand-alone μPID [18,41], which possesses a single-digit-picogram detection limit, and that the peak widths detected by iCPID were narrower than those by the off-chip stand-alone μPID due to the monolithic integration. Finally, an ultracompact, fully-automated,

Table 1
Comparison of μGC systems and modules.

μGC integration	Monolithic or hybrid	System or module	System size and weight	Battery- or wall-powered	Carrier gas	Detector	Microfabricated components and their integration
Grag et al. [34]	Monolithic	1D system	4.5 L and 1.8 kg	Battery	Helium	TCD	Precon., TCD integrated on column
Akbar et al. [32]	Monolithic	1D module	N/A*	N/A	Helium	μDPID	Sampling loop, μDPID integrated on column
Qin et al. [2]	Hybrid	1D module	N/A	N/A	Air**	Capacitive detector	Pump, precon., column, and capacitive detector
Liao et al. [16]	Monolithic	1D system	4.8 L, no weight reported	Battery	Air**	Capacitive detector and AiPD	Precon., column, AiPD and capacitive detector integrated using epoxy gluing on the same chip
Wang et al. [3]	Hybrid	1D system	2.7 L and 2.1 kg (sans battery)	Battery	Helium	Chemiresistor array	Precon., column, and chemiresistor array
Collin et al. [12]	Hybrid	1D system	12.4 L and 5.4 kg	Wall	Air**	Chemiresistor array	Precon., column, and chemiresistor array
Li et al. [18]	Hybrid	1D system	6.5 L, no weight reported	Wall	Helium	μPID	Column and μPID
Collin et al. [37]	Hybrid	2D module	N/A	N/A	Helium	Benchtop FID	Thermal modulator, columns
Whiting et al. [38]	Hybrid	2D module	N/A	N/A	Helium	Benchtop FID	Pneumatic modulator, columns
Lee et al. [20]	Hybrid	2D system	30 L and 5 kg	Wall	Helium	μPID	Precon., column, Deans switch, and μPID
Huang et al. [17]	Monolithic	2D system	8.4 L and 2.4 kg	Wall	Helium	μPID	1D column, pneumatic modulator integrated on 2D column, μPID
Zampolli et al. [25]	Hybrid	1D system	0.72 L (GC/PID), no weight reported	Wall	Helium (TCD); air (PID)**	TCD and PID	Precon., injector, column, TCD
You et al. [21]	Hybrid	1D system	15.7 L and 5 kg (sans battery)	Battery	Air**	PID	No microfabricated components
This work	Monolithic	1D system	0.9 L and 0.9 kg ***	Battery	Air**	iCPID	iCPID (integrated column and μPID)

* not applicable as a module.
** "Air" denotes operation without a gas cartridge.
*** including 0.45 kg batteries and associated electronics in a 0.34 L battery chamber.

battery-powered μGC system was constructed based on the iCPID. The entire system was self-contained within a 3D-printed box with a volume of only 0.9 liters and a weight of 0.9 kg and used ambient air as the carrier gas. A rapid separation of eight VOCs in two minutes isothermally at ambient temperature was demonstrated.

1.1. Integrated μcolumn and μPID (iCPID) device architecture and working principle

As illustrated in Fig. 1, the iCPID is fabricated on an SOI platform with a top-down architecture, where the μPID (in the device layer) resides on top of the μcolumn (in the handle layer). At the inlet and outlet of the μPID, there are two etched-through vertical pass-through holes that termed as "microfluidic vias". The first one connects the upstream μcolumn (in the handle layer) to the μPID (in the device layer) and the second one is routed towards the outlet of the iCPID (in the handle layer). The μPID and μcolumn are electrically isolated by the buried oxide (BOX) on SOI. A glass layer is anodically bonded to the SOI to seal the μcolumn. The heater of μcolumn is patterned on top the device layer of the SOI with an additional layer of SiO_2 to provide electrical isolation. A VUV lamp (Krypton for 10.6 eV or Argon for 11.7 eV) is hermetically mounted on the μPID by epoxy and serves as the photoionization source. To prevent outgassing from the epoxy used in lamp packaging, a micromachined insulation silicon wedge (inset of Fig. 1 (B)) is inserted to the side of microfluidic vias before applying epoxy. The monolithic batch microfabrication process of iCPID is depicted in Fig. 2 and described in "Experimental".

During operation, the gas mixture enters the inlet of the iCPID, and is subsequently separated by the μcolumn whose temperature is ramped by the integrated heater. Towards the end of the μcolumn, the separated molecules flow up through the microfluidic via and are then detected by the μPID before flowing back down towards the outlet of the iCPID. This top-down architecture of the iCPID minimizes the overall footprint by allowing the μPID to be stacked directly on the μcolumn while avoiding any interconnection in between. It also takes advantage of flow-through and nondestructive nature of the μPID, which allows for further downstream analysis (such as connecting the outlet of the iCPID to a 2nd-dimensional column [17]).

2. Experimental

2.1. Materials

Analytical standard-grade benzene, hexamethyldisilazane (HMDS), and the eight VOCs listed in Supplementary Table S1 were purchased from Sigma-Aldrich (St. Louis, MO). 400 μm thick, double-side polished Si wafers (<100 >, p-type, 0.001–0.005 Ω*cm and <100 >, p-type, 1–10 Ω*cm) were purchased from Ultrasil LLC. 550 μm Borofloat 33 glass (P/N 517) were purchased from UniversityWafer. A 10.6 eV VUV Kr lamp with a MgF_2 window was purchased from Mocon-baseline (P/N 043–257). Guard columns for fluidic packing and interconnections were purchased from Restak (P/N 10011). UV curable epoxy (NOA 68 T) was purchased from Norland Product Inc. Carbopacks B (P/N 20273) and X (P/N 10437-U) were purchased from Sigma-Aldrich. Additional accessory materials that used to build the system are provided in Table S2. All materials were used as purchased without further purification or modification.

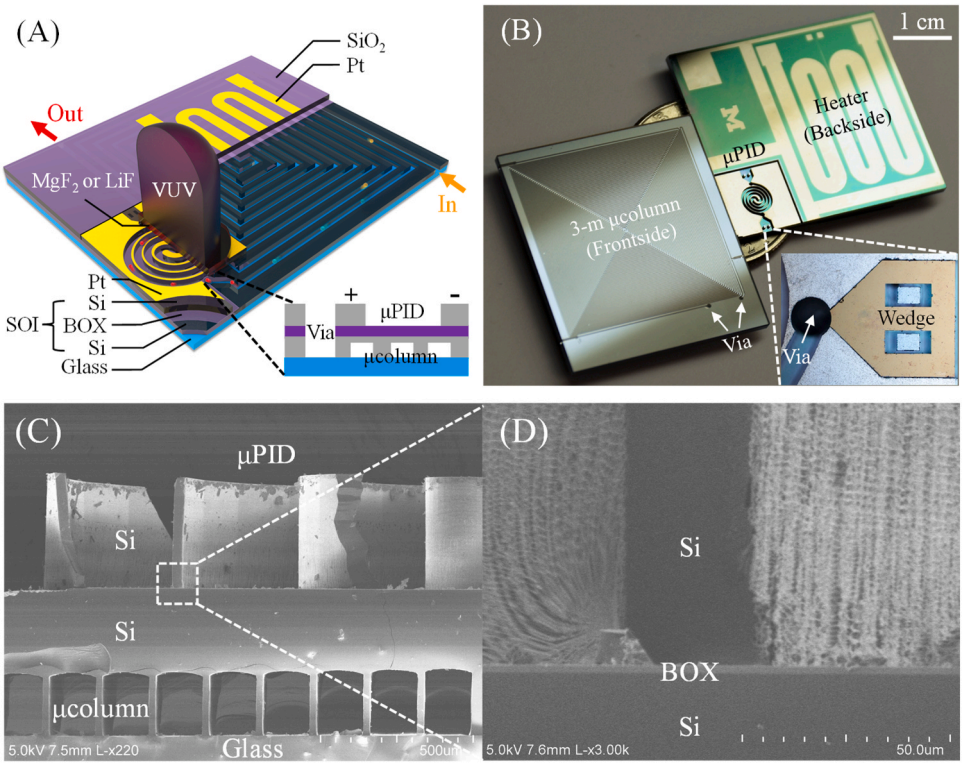

Fig. 1. (A) Architecture of the microfluidically integrated μcolumn and μPID (iCPID) device. The iCPID is constructed on a silicon-on-insulator (SOI) platform, where the device layer consists of a μPID and a heater for μcolumn heating, while the handle layer comprises a μcolumn capped with a glass layer. Zoom-in vertical structure shows that etched-through vertical microfluidic vias fluidically connect the μcolumn and μPID, while buried oxide (BOX) electrically isolates them. A vacuum ultraviolet (VUV) lamp (with a MgF_2 or LiF window) is hermetically packaged on the μPID using epoxy. The gas inlet and outlet are indicated. (B) Photograph of iCPIDs (left: 3-m μcolumn side up; right: μPID and heater side up). Inset shows an insulated silicon wedge filling up the etched-through channel opening at the inlet and outlet of the μPID to prevent exposure to epoxy during packaging. The holes of the wedge are aligned with the standing posts of the μPID to ensure proper alignment. (C) Scanning electron microscopy (SEM) of a cross-section of the iCPID featuring microfluidically integrated μPID on μcolumn. (D) Zoom-in view of the SOI structure.

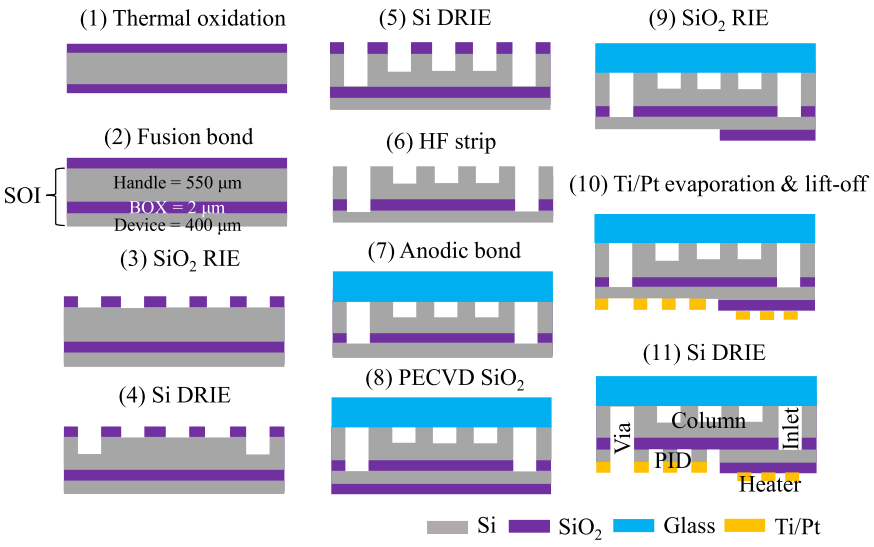

Fig. 2. Schematics outlining the microfabrication process for iCPID. (1) Thermal oxide was grown on a Si wafer. (2) An SOI wafer was created by fusion bonding the oxidized wafer to a highly doped Si wafer. The conductive wafer serves as the device layer and the oxidized wafer serves as the handle layer. (3) The oxide on the handle layer was patterned via photolithography and RIE to create a hard mask for the µcolumn, inlets, and pass-through microfluidic vias. (4) The inlets and pass-through vias were etched with DRIE while the µcolumn was protected with photoresist. (5) After stripping the photoresist, DRIE was continued using the oxide hard mask to etch the µcolumn while the inlets and pass-through vias were etched to the buried oxide layer (BOX). (6) Hydrofluoric acid (HF) was used to strip the thermal oxide hard mask and BOX in the pass-through vias. (7) The etched handle layer was anodically bonded to a borofloat glass wafer to seal the µcolumn. (8) Plasma-enhanced chemical vapor deposition (PECVD) was used to deposit a layer of SiO_2 on the device layer. (9) Photolithography was used to define the µPID region where the oxide was etched by RIE. (10) A layer of Ti/Pt was patterned on the device layer using lithography, evaporation, and liftoff to define the µPID electrodes and µcolumn heater simultaneously. (11) Patterned photoresist was used as a mask for the DRIE on the device layer to generate the µPID. The µPID was etched down to the BOX. After removing the photoresist, the wafer was diced into individual devices.

2.2. Microfabrication of iCPID

The monolithic microfabrication process for the iCPID is outlined in Fig. 2. Both wafers first underwent RCA clean. After a dielectric barrier discharge (DBD) of atmospheric N_2 plasma treatment on the bonding side of both wafers, a 400 µm thick, double-side polished Si wafer (<100 >, p-type, 0.001–0.005 Ω*cm) was fusion bonded [42] to a 550 µm thick, double-side polished Si wafer (<100 >, p-type, 1–10 Ω*cm) with 2 µm thick thermal oxide under vacuum at 400°C and 20 MPa for 4 hours to generate the SOI wafer where the conductive wafer serves as the device layer and the insulating wafer serves as the handle wafer. The oxide on the handle layer was then patterned using photolithography and reactive ion etching (RIE) to create a hard mask for the µcolumn (3 m in length x 150 µm in width with 30 µm thick walls), inlets (400 µm in width), and pass-through microfluidic vias (550 µm in diameter). Next, photolithography was used to selectively expose the inlets and pass-through vias for a deep reactive-ion etching (DRIE) etch of ~150 µm in depth. The photoresist was then stripped and DRIE continued with the hard mask to simultaneously etch the µcolumn to a final depth of 250 µm while the inlets and pass-through vias were etched to the buried oxide layer (BOX), which serves as the etch-stop, with the final depth of 400 µm. After stripping the thermal oxide and BOX on the pass-through vias with HF, the handle layer was anodically bonded [43] to a 550 µm thick borofloat glass wafer to seal the µcolumn after piranha-cleaned. Next, 1 µm of SiO_2 was deposited on the device layer by plasma-enhanced chemical vapor deposition (PECVD) and photolithography was used to define the µPID electrodes where the oxide is etched by RIE for depositing Pt thin films to form ohmic contact on the silicon electrodes and isolate the µPID from the rest of the device layer (with PECVD oxide). The defined area is shown in Fig. 1(B) where µPID's Pt electrodes reside. The photoresist was then stripped and a layer of Ti/Pt (30/360 nm) was patterned on the device layer using lithography, evaporation, and liftoff to define the µPID electrodes and µcolumn heater simultaneously. Finally, photoresist was used as a mask for the DRIE on the device layer to generate the µPID (400 µm wide channels in an Archimedean spiral with 40 µm thick walls and a length of 3.2 cm). The µPID was etched down to the BOX (etch-stop). After removing the photoresist, the wafer was diced into individual devices with dimensions of 26.4 mm×29.6 mm×1.5 mm (length x width x thickness).

2.3. Microfluidic and electrical packaging of iCPID

For hermatically packaging the VUV lamp on the integrated µPID using UV epoxy, a customized silicon wedge was fabricated to underfill the etched-through inlet and outlet near the microfludic vias before applying the UV epoxy to avoid possible clotting and outgasing from the epoxy. The insulated wedges shown in the inset of Fig. 1(B) were microfabricated using a 400 µm thick, double-side polished Si wafer that were first diced into 2 cm by 2 cm pieces. Then the piece was patterned and etched through to generate the free-standing wedges. The wedges were then conformally coated with 200 nm of SiO_2 by atomic layer deposition (ALD) for insulation. It should be noted that the ALD process was chosen for its ability to achieve the best conformal coating along the sidewall, although sputtering was also used to achieve the same purpose.

The coating procedure of the µcolumn in the iCPID is illustrated Figure S1. First, the guard columns were inserted into the inlet and outlet of the iCPID as well as the coating outlet port. Prior to coating, the µcolumn was deactivated by eight repeated injections of HMDS into the column inlet (*i.e.*, coating inlet) at 120 °C within 1 hour, and the coating outlet was blocked with a rubber septum during deactivation. Next, the coating outlet was hermetically connected to a vial that was linked to a pump. A coating solution (2% (w/w) of OV-5 in dichloromethane) of 100 µL was then injected from the coating inlet and dynamically coated into the 3 m µcolumn. The pump's pulling mechanism ensures the coating solution to bypass the µPID downstream. The coating rate was controlled by adjusting the voltage of the pump, which was set at 5 cm/min. The coating process was repeated 3 times. The µcolumn was subsequently treated with HMDS after each coating and then baked at 180 °C for 1 hour prior to use. The coating solution was then drained

into the vial and can be recycled for further usage. Finally, the guard column attached to the coating outlet was removed, and UV epoxy was applied to block the outlet.

After the μcolumn coating, the iCPID was affixed to a printed circuit board (PCB), and the integrated μPID and heater were wire-bonded. The heater had a resistance of 50 Ohms. Next, the insulated wedges were fitted into the designated slots in front of the microfluidic vias in the μPID as shown in the inset of Fig. 1(B). Finally, a 10.6 eV VUV Kr lamp was assembled on top and hermetically secured by UV epoxy along the perimeter.

2.4. iCPID operation and characterization

Packaged iCPID was operated using a μGC system platform developed in our previous work [17] which was controlled by LabVIEW™ software developed in-house. A Keithley 2400 sourcemeter was used for alternating the bias voltage between μPID electrodes. The sensitivity evaluation was performed using an Agilent 6890 benchtop gas chromatography (GC) equipped with a thermal injector operated at 250 °C and in a split mode for controlling analyte injection amount. 99.999% Helium was used as the carrier gas with a flow rate of 3 mL/min. All measurements were done at room temperature with only guard columns for fluidic connections. The heater on iCPID was driven by 5-Hz pulse-width-modulation (PWM) through an NI DAQ card. A thermocouple was used to access the temperature measurement on chip.

3. Results and discussion

3.1. Characterization of iCPID VOC detection performance

As the integrated μPID on the iCPID device has the identical design as the glass substrate based stand-alone μPID [18,41], the latter is therefore used as a benchmark to evaluate iCPID's sensitivity and is referred to as "benchmark μPID". The benchmark μPID was shown to have a single-digit-picogram detection limit with approximately six orders of magnitude linear dynamic range up to 1000 ng [41]. As shown in Fig. 3 (A), to ensure an accurate comparison, the iCPID were fluidically connected in series after the benchmark μPID owing to its flow-through nature. The analytes flowed through the benchmark μPID first and then the μPID on the iCPID, and finally vented out through the μcolumn on the iCPID. Such arrangement eliminates any interference effects caused by the downstream integrated μcolumn (such as peak broadening) so that the intrinsic response of the integrated μPID on the iCPID can be revealed. As shown in Figure S2, the iCPID has the same peak shape as the benchmark μPID as expected. Fig. 3(B) depicts the comparison between the response (area under a peak) of the integrated μPID on the iCPID against the benchmark μPID. Using the unity line as the reference, the integrated μPID demonstrated a sensitivity similar to the benchmark μPID at lower injection masses (*i.e.*, benchmark μPID peak area <1 V*s, equivalent to <1 ng) without any bias voltage dependence. However, at higher injection masses, the integrated μPID's response was observed to be sublinear and the sublinearity became more pronounced with decreasing bias voltages. The baseline noise remained similar (~1 mV) to the benchmark μPID (1.9 mV) at lower bias voltages (below 8 V) but increased superlinearly up to ~40 mV at high voltages, as shown in the inset of Fig. 3(B). The cause of the deviated performances of the integrated μPID from the benchmark μPID was attributed to the BOX layer within the SOI that is presumed to be electrically insulated became leaky after fusion bonding [44] (see Section S3 for details). The leakage reduces the effective electric field generated by the parallel plates to efficiently capture the generated ions within the photoionization chamber, particularly at a high analyte concentration and a low bias voltage, and meanwhile, increases the noise when the bias voltage is high (>10 V).

In practice, the integrated μPID on the iCPID should therefore be operated at low bias voltages (*e.g.*, 6–10 V), which can still achieve low noise levels with a single digit picogram detection limit and good linearity at low analyte concentrations. At higher analyte concentrations, its sublinear response requires pre-calibration by a benchmark detector prior to use when quantitative measurement is desired. For future iterations of the iCPID, alternative microfabrication processes that produce SOI wafers with truly insulated BOX, such as separation by implantation of oxygen (SIMOX) [45,46], are worth exploring.

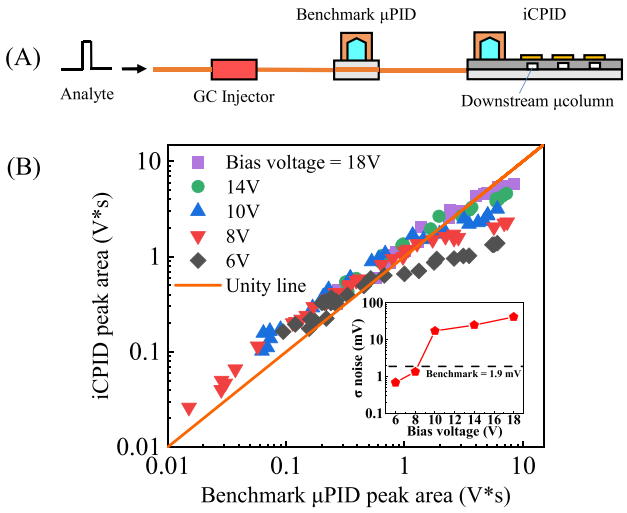

Fig. 3. (A) Setup to evaluate the performance of the integrated μPID on iCPID using a stand-alone glass substrate based μPID [41] as benchmark (biased constantly at 24 V). The test analyte (benzene) was injected via a bench-top GC injector. The flow-through benchmark μPID was connected in series with iCPID with μcolumn downstream. Note that in this particular setup, the analyte entered the integrated μPID on iCPID before reaching the μcolumn on iCPID to avoid any effects caused by the μcolumn. Helium was used as the carrier gas with a flow rate of 3 mL/min. (B) Log-log plot of iCPID peak area (biased from 6 to 18 V) as a function of benchmark μPID peak area. Each data point represents the respective responses of iCPID and benchmark μPID to the same single injection. The peak area of the benchmark μPID, ranging from 0.01 to 10 V*s, was calibrated to be associated with an injection mass of 0.13 ng to 130 ng, which falls within its linear response regime [41]. The inset in (B) depicts the one sigma noise of iCPID biased at different voltages. The black dashed line indicating the noise level of the benchmark μPID measured concurrently.

3.2. Thermal crosstalk between integrated μPID and integrated heater on iCPID

Microfluidic integration introduces inherent thermal crosstalk between the integrated μPID and heater on μcolumn. First, the heat transfer in the iCPID was studied. As illustrated in Fig. 1(B), the integrated heater only covers two thirds of the area of the iCPID chip. We can therefore divide the chip territory into three different regions: (A) part of the μcolumn with the integrated heater directly on its back, (B) part of the μcolumn without the integrated heater on its back, and (C) the μPID that does not have the integrated heater. Since the μPID region cannot be directly accessed by a thermocouple after packaging a VUV lamp on top, temperatures of an unpackaged iCPID at three different regions were simultaneously measured during temperature ramping using the integrated heater, as shown in Fig. 4(A). Both the measured and simulated temperature profiles indicate that the temperature at regions B and C ramps almost the same as region A (*i.e.*, the μcolumn with a heater on its back). The difference is only a few °C at most, suggesting that the region of the μcolumn without a heater at the backside can be adequately heated for efficient separation, but at the cost of inevitable thermal crosstalk to the microfluidically integrated μPID.

To evaluate the impact of thermal crosstalk on the sensitivity of the

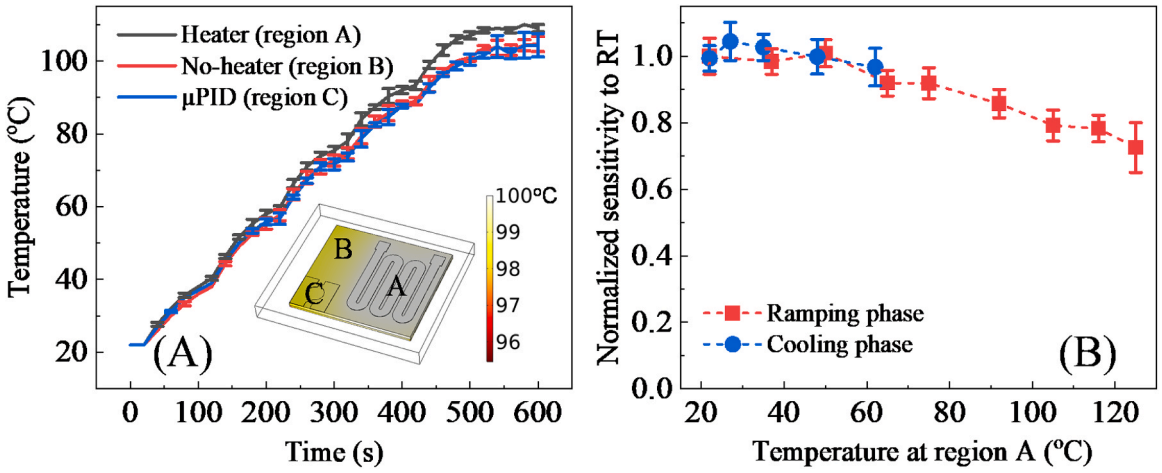

Fig. 4. (A) Measured temperature ramping profiles at the μcolumn with (A) and without (B) the integrated heater, and μPID (C). The inset displays a simulated temperature profile of the iCPID with the integrated heater set to 100 °C (see S3 in the Supplemetry Information for simulation details). (B) Normalized sensitivity (relative to room temperature) of the integrated μPID as a function of the temperature measured at region A on the chip during both ramping and cooling phases, respectively. Error bars were obtained from three measurements.

integrated μPID, we employed the same setup as in Fig. 3(A) while maintaining the benchmark μPID at room temperature as the control to calibrate the sensitivity change in the temperature-ramped iCPID. Fig. 4 (B) shows that the sensitivity of the integrated μPID remained relatively stable during the initial ramp phase (>92% up to 75 °C), which is in agreement with our previous report [41], before gradually decreasing to ~75% at 125 °C. This sensitivity reduction was reversible, *i.e.*, the integrated μPID sensitivity returned to the normal level when the temperature went back to room temperature. The reduction in sensitivity at high temperatures can primarily be attributed to changes in the VUV photoionization source, including transmission and generation. First, the VUV lamp window's short-wavelength transmittance limit (116 nm or 10.6 eV for MgF_2 in this case) red-shifts as it is heated [47,48], resulting in lower transmission for high-energy VUV photons available for photoionization. Second, VUV photon generation from plasma is an isometric process inside the VUV lamp housing. The temperature increase causes a higher pressure (per ideal gas law), resulting in more collisions and hence more de-excitation of the particles capable of emitting VUV photons.

3.3. Characterization of iCPID VOC separation performance

The separation performance of the iCPID was evaluated using the setup illustrated in Fig. 5(A) (note the μcolumn of iCPID was connected upstream in contrast to Fig. 3(A)). To compare the peak shape difference between on- and off-chip detection, an off-chip stand-alone μPID was connected to the outlet of the iCPID through a 20-cm guard column as interconnection. We selected the BTEX mixture (*i.e.*, benzene, toluene, ethylbenzene, and p-xylene) as the model analytes. Note that as the off-chip stand-alone μPID was connected in series as the benchmarking for relative performance comparison to the on-chip μPID, the actual BTEX mixture concentrations were irrelevant and therefore were not calibrated (as long as they were kept in the linear region of μPID) for simplicity. The iCPID was operated isothermally at room temperature (*i.e.*, without temperature ramp) to simulate a field operation scheme with low power consumption.

As shown in Fig. 5(B), BTEX were effectively separated by the 3-m OV-5 integrated μcolumn with height equivalents to theoretical plate (HETP) values of 3.5 mm (benzene), 3.0 mm (toluene), 2.6 mm (ethylbenzene), and 2.4 mm (p-xylene). The off-chip stand-alone μPID detected a similar chromatogram with broader peak width for each peak. For example, the inset of Fig. 5(B) shows that the on-chip detection rendered a toluene peak 0.6 s narrower in full-width-half-maximum (FWHM)

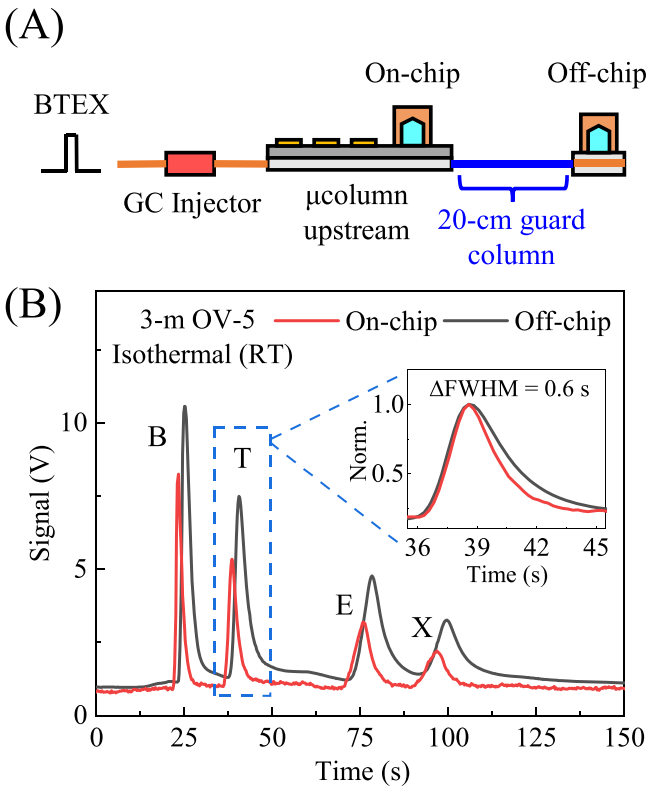

Fig. 5. (A) Setup to evaluate the separation performance of the 3-m OV-5 integrated μcolumn on the iCPID using on-chip integrated μPID and off-chip benchmark μPID. The BTEX mixture was injected via a bench-top GC injector. The integrated μcolumn was fluidically connected upstream and operated isothermally at room temperature. 20-cm guard column was used as the in-series fluidic interconnection between the iCPID and the off-chip stand-alone μPID. Helium was used as the carrier gas with a flow rate of 1 mL/min. (B) Chromatograms of BTEX generated using the iCPID and the off-chip benchmark μPID. The inset shows the zoom-in view of normalized toluene peaks detected by on-chip and off-chip μPIDs, respectively. The retention times (peak apexes) are aligned with each other for clarity.

than the off-chip detection. The corresponding differences for benzene, ethylbenzene, and p-xylene are 0.7 s, 1 s, and 0.5 s, respectively. The peak broadening effect can be attributed to the 20-cm interconnecting guard column between the iCPID and off-chip μPID. These results manifest the advantage of microfluidic integration of μcolumn and μPID by eliminating transfer lines in between. The temperature ramped effect on peak width is examined in Figure S8. It is observed that both on-chip and off-chip detection peak widths decrease due to the increased column temperature on iCPID (from room temperature to 55 °C). However, the off-chip detection peak width is broadened 20–30% over the on-chip detection peak width,

For a further benchmarking comparison, the BTEX mixture was also separated using a commercial 3-m OV-5 column with off-chip μPID detection at room temperature (Figure S9). The HETP values of benzene (35.4 mm) and toluene (7.4 mm) in the commercial column were found to be significantly larger than those in iCPID due to broader peak widths in commercial columns. Additional full-width-half-maximum (FWHM) of 4 s and 3.4 s were observed for benzene and toluene peaks, respectively. However, the HETP values of ethylbenzene (2.2 mm) and p-xylene (1.8 mm) were similar to those in the iCPID as their respective retention times in the commercial column were much longer. Both the broader peak widths in the early two peaks and longer retention times in the latter two can be attributed to the thicker coating of the commercial column (0.25 μm) than the integrated μcolumn (~0.1 μm [49]). Table S3 summarizes the detailed characteristics of the commercial column and the iCPID with on- and off-chip detection.

3.4. Construction and characterization of an ultracompact μGC system based on iCPID

We built an ultracompact μGC system based on the iCPID, dubbed integrated cube (*i.e.*, iCube). The components and fluidic diagram for the iCube along with its operation and photo are presented in Fig. 6(A) and (B). The iCube was constructed in a 3D-printed three-layered closed-box structure, featuring a top-down configuration wherein each layer accommodated specific components (Figure S5). The system consisted mainly of a stainless steel preconcentrator, an iCPID, a pump, an air filter, two microfabricated Y-connectors (for compactness), two 3-port valves, a set of four 5500 mAh rechargeable batteries and an in-house control circuit board. Components were fluidically interconnected using flexible Polytetrafluoroethylene (PTFE) tubes and guard columns. Bias voltage for iCPID was set to 6 V to optimize the signal to noise ratio of the system. To further minimize the noise, copper mesh shields were used inside the enclosure to cover the system and major electromagnetic interference (EMI)-prone electrical components. The total size of the iCube was 0.9 L (108 mm×94 mm x 85 mm (length x width x height)) and weighed only 0.9 kg, including 0.45 kg batteries and associated electronics in a 0.34 L battery chamber.

For iCube operation, the analytes were sampled from a gas storage bag into the preconcentrator before backflush injection into the iCPID (see the red analyzing path). Ambient air, which was filtered through an inline filter to remove moisture and hydrocarbons, was used as the carrier gas at a flow rate of ~0.9 mL/min. The sampling rate of iCube was ~8 mL/min. Separation was conducted isothermally at room

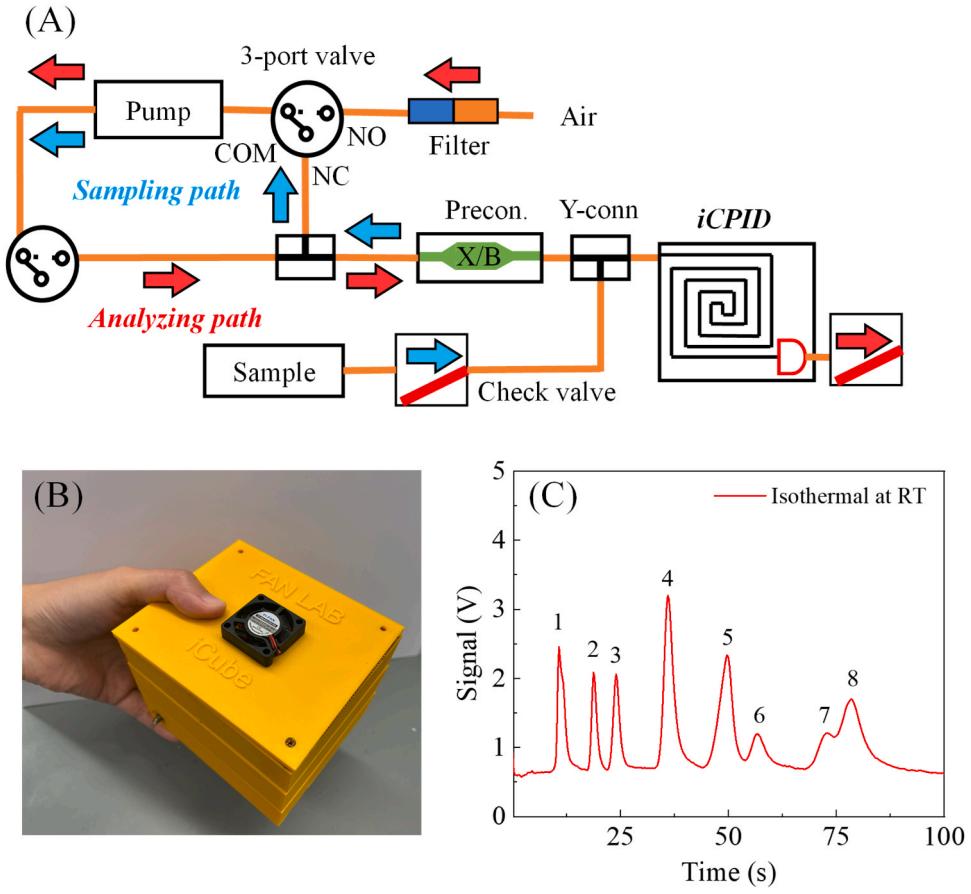

Fig. 6. (A) System schematic of the ultracompact μGC device, named integrated Cube (*i.e.*, iCube). X and B: Carbopack X and B. COM: common; NO: normally-open; NC: normally-closed; the sampling and analyzing path are indicated with blue and red arrows respectively. (B) Photograph of the iCube that occupies 0.9 L and weighs 0.9 kg. (C) Chromatogram of (1) acetone, (2) benzene, (3) heptane, (4) toluene, (5) octane, (6) butyl acetate, (7) ethylbenzene, and (8) xylene generated by the iCube. Filtered air was used as the carrier gas with a flow rate of 0.9 mL/min. Separation was conducted isothermally at 22 °C. Repeatability tests can be found in Fig. S12.

temperature (~22 °C). A representative chromatogram of a standard sample containing eight VOCs (listed in Table S1) is shown in Fig. 6(C), showing that separation can be completed within 100 s. Energy consumption of the iCube was 2.53 kJ per run assuming a 6-minute operation time, which led to an estimated total working cycle of 110 (Table S4). In practice, we performed a continuous repeated operation of the iCube for up to 20 cycles as shown in Figure S12. It was observed that after a ~4-cycle of "warm-up" operation (~10 minutes of warm-up time), the system maintained stable chromatographic performance (*i.e.*, peak height, retention time, FWHM, *etc*.).

The iCube features some combined advantages of recent μGC systems and modules in a few aspects as listed in Table 1. Note that the term "monolithic" used in the table indicates partial integration between two or more discrete components but not entire system. First, the iCPID eliminates the use of interconnects between the column and the detector, resulting in easier manufacturing and assembly as well as reduction in overall system volume, and it also increases robustness of the fluidic connections and hence better overall system operational reliability compared to using all stand-alone microfabricated components in hybrid integration. In addition, microfluidic integration also eliminates the potential cold spots between the column and the detector, leading to narrower chromatographic peaks. Second, the iCube utilizes ambient air as carrier gas to avoid the need for a helium cartridge, which inevitably increases the footprint, weight, and maintenance effort (*i.e.*, replacing cartridges) of the entire system. Third, the iCube utilizes batteries, which further improves its mobility. Note that the battery set actually occupied one third of the total weight and volume of the iCube. Further reducing them to a smaller footprint without sacrificing the power specifications can result in an even more compact system.

4. Conclusion

This article presents a microfluidically integrated photoionization detector (μPID) on a microfabricated gas chromatography (μGC) column. The parallel-plate silicon electrodes of the μPID and the μcolumn were monolithically fabricated via wafer-level batch processing on an SOI platform, realizing microfluidic integration between the μPID and μcolumn which were previously connected off-chip through hybrid integration. The integrated chip enables an ultracompact (0.9 L and 0.9 kg), fully automated, and battery-operated μGC system. Rapid separation of eight volatile organic compounds (VOCs) in ~2 min at room temperature was demonstrated. Future work includes modified processes that can resolve the leakage in BOX, better thermal management on-chip, and new device architectures that can incorporate preconcentrators to realize "all-in-one" monolithic μGC platform. Such integration schemes are also possible to be applied to multi-dimensional μGC architectures with integrated modulators on the same chip.

CRediT authorship contribution statement

Xiaheng Huang: Writing – original draft, Methodology, Investigation, Formal analysis, Data curation, Conceptualization. **Shuo Yang:** Writing – original draft, Formal analysis, Data curation, Conceptualization. **Wencheng Li:** Writing – original draft, Formal analysis, Data curation. **Robert Nidetz:** Writing – original draft, Methodology, Data curation. **Ruchi Sharma:** Writing – original draft, Data curation. **Anjali Devi Sivakumar:** Writing – original draft, Formal analysis, Data curation. **Chandrakalavathi Thota:** Writing – original draft, Formal analysis, Data curation. **Hongbo Zhu:** Conceptualization. **Weishu Wu:** Writing – original draft, Data curation. **Seong-Yong Jeong:** Data curation. **Xudong Fan:** Writing – original draft, Supervision, Resources, Project administration, Funding acquisition, Formal analysis, Conceptualization.

Declaration of Competing Interest

The authors declare the following financial interests/personal relationships which may be considered as potential competing interests: The photoionization detector (PID) technology used in the article is licensed to Nanova, RUA Diagnostics, and ChromX Health. Hongbo Zhu and Xudong Fan are the co-inventors of this technology and have financial interest in the above companies. Xudong Fan also serves as a paid or unpaid consultant to these companies

Data availability

Data will be made available on request.

Acknowledgments

The authors acknowledge the support from National Institute for Occupational Safety and Health (NIOSH) via R01 OH011082–01A1 and the Office of the Director of National Intelligence (ODNI), Intelligence Advanced Research Projects Activity (IARPA), via IARPA FA8650–19-C-9101. The views and conclusions contained herein are those of the authors and should not be interpreted as necessarily representing the official policies or endorsements, either expressed or implied, of the ODNI, IARPA, or the U.S. Government. The U.S. Government is authorized to reproduce and distribute reprints for Governmental purposes notwithstanding any copyright annotation thereon. The authors acknowledge microfabrication aid from the Lurie Nanofabrication Facility. The authors acknowledge Subhajit Mohanty, Xin Zhai, and Prof. Elaheh Ahmadi for probe station access.

Appendix A. Supporting information

Supplementary data associated with this article can be found in the online version at doi:10.1016/j.snb.2024.135717.

References

[1] B.P. Regmi, M. Agah, Micro gas chromatography: an overview of critical components and their integration, Anal. Chem. *90* (22) (2018) 13133–13150.
[2] Y. Qin, Y.B. Gianchandani, A fully electronic microfabricated gas chromatograph with complementary capacitive detectors for indoor pollutants, Microsyst. Nanoeng. *2* (1) (2016) 1–11.
[3] J. Wang, N. Nuñovero, R. Nidetz, S.J. Peterson, B.M. Brookover, W.H. Steinecker, E.T. Zellers, Belt-mounted micro-gas-chromatograph prototype for determining personal exposures to volatile-organic-compound mixture components, Anal. Chem. *91* (7) (2019) 4747–4754.
[4] J. Wang, J. Bryant-Genevier, N. Nuñovero, C. Zhang, B. Kraay, C. Zhan, K. Scholten, R. Nidetz, S. Buggaveeti, E.T. Zellers, Compact prototype microfabricated gas chromatographic analyzer for autonomous determinations of VOC mixtures at typical workplace concentrations, Microsyst. Nanoeng. *4* (1) (2018) 1–10.
[5] S.K. Kim, H. Chang, E.T. Zellers, Microfabricated gas chromatograph for the selective determination of trichloroethylene vapor at sub-parts-per-billion concentrations in complex mixtures, Anal. Chem. *83* (18) (2011) 7198–7206.
[6] R. Sharma, W. Zang, A. Tabartehfarahani, A. Lam, X. Huang, A.D. Sivakumar, C. Thota, S. Yang, R.P. Dickson, M.W. Sjoding, Portable breath-based volatile organic compound monitoring for the detection of COVID-19 during the circulation of the SARS-CoV-2 delta variant and the transition to the SARS-CoV-2 omicron variant, JAMA Netw. Open *6* (2) (2023) e230982-e230982.
[7] M. Zhou, R. Sharma, H. Zhu, Z. Li, J. Li, S. Wang, E. Bisco, J. Massey, A. Pennington, M. Sjoding, Rapid breath analysis for acute respiratory distress syndrome diagnostics using a portable two-dimensional gas chromatography device, Anal. Bioanal. Chem. *411* (2019) 6435–6447.
[8] R. Sharma, W. Zang, M. Zhou, N. Schafer, L.A. Begley, Y.J. Huang, X. Fan, Real time breath analysis using portable gas chromatography for adult asthma phenotypes, Metabolites *11* (5) (2021) 265.
[9] D. Lindner, The mChemLab™ project: micro total analysis system R&D at Sandia National Laboratories, Lab Chip *1* (1) (2001) 15N–19N.
[10] G. Frye-Mason, R. Kottenstette, P. Lewis, E. Heller, R. Manginell, D. Adkins, G. Dulleck, D. Martinez, D. Sasaki, C. Mowry, Hand-held miniature chemical analysis system (μChemLab) for detection of trace concentrations of gas phase analytes. Micro Total Analysis Systems 2000: Proceedings of the μTAS 2000 Symposium, held in Enschede, The Netherlands, 14–18 May 2000, Springer, 2000, pp. 229–232.

[11] B. Kaanta, H. Chen, X. Zhang, Monolithic micro gas chromatographic separation column and detector. 2010 IEEE 23rd International Conference on Micro Electro Mechanical Systems (MEMS), IEEE, 2010, pp. 907–910.
[12] W.R. Collin, G. Serrano, L.K. Wright, H. Chang, N. Nunovero, E.T. Zellers, Microfabricated gas chromatograph for rapid, trace-level determinations of gas-phase explosive marker compounds, Anal. Chem. *86* (1) (2014) 655–663.
[13] R.C. Blase, M.J. Libardoni, G.P. Miller, K.E. Miller, C.M. Phillips-Lander, C.R. Glein, J.H. Waite, A. Ghosh, A. Venkatasubramanian, M.W.H. Li, et al., MEMS GC column performance for analyzing organics and biological molecules for future landed planetary missions, Front. Astron. Space Sci. *9* (2022) 828103. DOI: ARTN 82810310.3389/fspas.2022.828103.
[14] R.C. Blase, M.J. Libardoni, G.P. Miller, K.E. Miller, C.M. Phillips-Lander, J. H. Waite, C.R. Glein, H. Zhu, A. Ghosh, A. Venkatasubramanian, Experimental coupling of a MEMS gas chromatograph and a mass spectrometer for organic analysis in space environments, ACS Earth Space Chem. *4* (10) (2020) 1718–1729.
[15] C.-J. Lu, W.H. Steinecker, W.-C. Tian, M.C. Oborny, J.M. Nichols, M. Agah, J. A. Potkay, H.K. Chan, J. Driscoll, R.D. Sacks, First-generation hybrid MEMS gas chromatograph, Lab a Chip *5* (10) (2005) 1123–1131.
[16] W. Liao, D. Winship, I. Lara-Ibeas, X. Zhao, Q. Xu, H.-T. Lu, T. Qian, R. Gordenker, Y. Qin, Y.B. Gianchandani, Highly integrated μGC based on a multisensing progressive cellular architecture with a valveless sample inlet, Anal. Chem. (2023).
[17] X. Huang, M.W.-h Li, W. Zang, X. Huang, A.D. Sivakumar, R. Sharma, X. Fan, Portable comprehensive two-dimensional micro-gas chromatography using an integrated flow-restricted pneumatic modulator, Microsyst. Nanoeng. *8* (1) (2022) 115.
[18] M. Wei-Hao Li, A. Ghosh, A. Venkatasubramanian, R. Sharma, X. Huang, X. Fan, High-sensitivity micro-gas chromatograph–photoionization detector for trace vapor detection, ACS Sens. *6* (6) (2021) 2348–2355.
[19] S.C. Terry, J.H. Jerman, J.B. Angell, A gas chromatographic air analyzer fabricated on a silicon wafer, IEEE Trans. Electron Devices *26* (12) (1979) 1880–1886.
[20] J. Lee, M. Zhou, H. Zhu, R. Nidetz, K. Kurabayashi, X. Fan, Fully automated portable comprehensive 2-dimensional gas chromatography device, Anal. Chem. *88* (20) (2016) 10266–10274.
[21] D.-W. You, Y.-S. Seon, Y. Jang, J. Bang, J.-S. Oh, K.-W. Jung, A portable gas chromatograph for real-time monitoring of aromatic volatile organic compounds in air samples, J. Chromatogr. A *1625* (2020) 461267.
[22] S. Zampolli, I. Elmi, F. Mancarella, P. Betti, E. Dalcanale, G. Cardinali, M. Severi, Real-time monitoring of sub-ppb concentrations of aromatic volatiles with a MEMS-enabled miniaturized gas-chromatograph, Sens. Actuators B: Chem. *141* (1) (2009) 322–328.
[23] T.-H. Tzeng, C.-Y. Kuo, S.-Y. Wang, P.-K. Huang, Y.-M. Huang, W.-C. Hsieh, Y.-J. Huang, P.-H. Kuo, S.-A. Yu, S.-C. Lee, A portable micro gas chromatography system for lung cancer associated volatile organic compound detection, IEEE J. Solid-State Circuits *51* (1) (2015) 259–272.
[24] Q. Zhong, W.H. Steinecker, E.T. Zellers, Characterization of a high-performance portable GC with a chemiresistor array detector, Analyst *134* (2) (2009) 283–293.
[25] S. Zampolli, I. Elmi, G.C. Cardinali, L. Masini, F. Bonafè, F. Zardi, Compact-GC platform: a flexible system integration strategy for a completely microsystems-based gas-chromatograph, Sens. Actuators B: Chem. *305* (2020) 127444.
[26] A. Ghosh, C.R. Vilorio, A.R. Hawkins, M.L. Lee, Microchip gas chromatography columns, interfacing and performance, Talanta *188* (2018) 463–492.
[27] A. Radadia, A. Salehi-Khojin, R. Masel, M. Shannon, The effect of microcolumn geometry on the performance of micro-gas chromatography columns for chip scale gas analyzers, Sens. Actuators B: Chem. *150* (1) (2010) 456–464.
[28] A. Ghosh, J.E. Johnson, J.G. Nuss, B.A. Stark, A.R. Hawkins, L.T. Tolley, B. D. Iverson, H.D. Tolley, M.L. Lee, Extending the upper temperature range of gas chromatography with all-silicon microchip columns using a heater/clamp assembly, J. Chromatogr. A *1517* (2017) 134–141.
[29] A.D. Radadia, R.I. Masel, M.A. Shannon, J.P. Jerrell, K.R. Cadwallader, Micromachined GC columns for fast separation of organophosphonate and organosulfur compounds, Anal. Chem. *80* (11) (2008) 4087–4094.
[30] R.P. Manginell, J.M. Bauer, M.W. Moorman, L.J. Sanchez, J.M. Anderson, J. J. Whiting, D.A. Porter, D. Copic, K.E. Achyuthan, A monolithically-integrated μGC chemical sensor system, Sensors *11* (7) (2011) 6517–6532.
[31] K. Reddy, J. Liu, M.K.K. Oo, X. Fan, Integrated separation columns and Fabry-Pérot sensors for microgas chromatography systems, J. Micro Syst. *22* (5) (2013) 1174–1179.
[32] M. Akbar, M. Restaino, M. Agah, Chip-scale gas chromatography: from injection through detection, Microsyst. Nanoeng. *1* (1) (2015) 1–8.
[33] M. Akbar, H. Shakeel, M. Agah, GC-on-chip: integrated column and photoionization detector, Lab Chip *15* (7) (2015) 1748–1758.
[34] A. Garg, M. Akbar, E. Vejerano, S. Narayanan, L. Nazhandali, L.C. Marr, M. Agah, Zebra GC: A mini gas chromatography system for trace-level determination of hazardous air pollutants, Sens. Actuators B: Chem. *212* (2015) 145–154.
[35] S. Narayanan, M. Agah, Fabrication and characterization of a suspended TCD integrated with a gas separation column, J. Micro Syst. *22* (5) (2013) 1166–1173.
[36] Y. Sun, J. Liu, D.J. Howard, G. Frye-Mason, A.K. Thompson, S.-J. Ja, X. Fan, Rapid tandem-column micro-gas chromatography based on optofluidic ring resonators with multi-point on-column detection, Analyst *135* (1) (2010) 165–171.
[37] W.R. Collin, A. Bondy, D. Paul, K. Kurabayashi, E.T. Zellers, μGC× μGC: comprehensive two-dimensional gas chromatographic separations with microfabricated components, Anal. Chem. *87* (3) (2015) 1630–1637.
[38] J.J. Whiting, E. Myers, R.P. Manginell, M.W. Moorman, J. Anderson, C.S. Fix, C. Washburn, A. Staton, D. Porter, D. Graf, A high-speed, high-performance, microfabricated comprehensive two-dimensional gas chromatograph, Lab a Chip *19* (9) (2019) 1633–1643.
[39] H. Zhu, M. Zhou, J. Lee, R. Nidetz, K. Kurabayashi, X. Fan, Low-power miniaturized helium dielectric barrier discharge photoionization detectors for highly sensitive vapor detection, Anal. Chem. *88* (17) (2016) 8780–8786.
[40] M.W.-H. Li, A. Ghosh, R. Sharma, H. Zhu, X. Fan, Integrated microfluidic helium discharge photoionization detectors, Sens. Actuators B: Chem. *332* (2021) 129504.
[41] H. Zhu, R. Nidetz, M. Zhou, J. Lee, S. Buggaveeti, K. Kurabayashi, X. Fan, Flow-through microfluidic photoionization detectors for rapid and highly sensitive vapor detection, Lab a Chip *15* (14) (2015) 3021–3029.
[42] Q.-Y. Tong, U. Goesele, Semiconductor Wafer Bonding: Science and Technology, John Wiley, 1999.
[43] E. Tatar, M. Torunbalci, S. Alper, T. Akin, A method and electrical model for the anodic bonding of SOI and glass wafers. 2012 IEEE 25th International Conference on Micro Electro Mechanical Systems (MEMS), IEEE, 2012, pp. 68–71.
[44] V. Afanas' ev, P. Ericsson, S. Bengtsson, M.O. Andersson, Wafer bonding induced degradation of thermal silicon dioxide layers on silicon, Appl. Phys. Lett. *66* (13) (1995) 1653–1655.
[45] H. Fujioka, Method of manufacturing semiconductor on insulator, Google Pat. (1991).
[46] G.K. Celler, S. Cristoloveanu, Frontiers of silicon-on-insulator, J. Appl. Phys. *93* (9) (2003) 4955–4978.
[47] W. Hunter, S. Malo, The temperature dependence of the short wavelength transmittance limit of vacuum ultraviolet window materials—I. Experiment, J. Phys. Chem. Solids *30* (12) (1969) 2739–2745.
[48] M.H. Reilly, Temperature dependence of the short wavelength transmittance limit of vacuum ultraviolet window materials—II theoretical, including interpretations for UV spectra of SiO2, GeO2, and Al2O3. J. Phys. Chem. Solids *31* (5) (1970) 1041–1056.
[49] Zhu, H. Development of Micro Gas Chromatographs and Micro Photoionization Detectors. 2019.

Xiaheng Huang received B.E. in Optoelectronics from Tianjin University in 2016, and Ph. D. in Electrical Engineering from the University of Michigan, Ann Arbor in 2023. Currently, he is a Principle Engineer at Corporate Research, Taiwan Semiconductor Manufacturing Company (TSMC) in San Jose, CA.

Shuo Yang received a B.E. from Donghua University in 2015, and Ph.D. from Missouri University of Science and Technology in 2021. Currently he is a postdoctoral research fellow at the University of Michigan.

Wencheng Li Wencheng Li received a B.E. from Tianjin University in 2022. Currently she is a master student in the Electrical Engineering and Computer Science Department at the University of Michigan.

Robert Nidetz obtained a B.S. in Materials Science and Engineering from the University of Illinois at Urbana/Champaign in 2006 and an M.S. and Ph.D. in Materials Science and Engineering from the University of Michigan in 2009 and 2011. Between 2011 and 2013 he worked as a Senior MEMS Engineer designing, microfabricating, and testing MEMS devices. From late-2013–2016, he was a postdoctoral researcher in Mechanical Engineering at the University of Michigan investigating microfluidic immunophenotyping devices and micro-gas chromotagoraphy components. In 2019 he obtained an M.S. in Secondary Education and Teaching from the University of Alabama at Birmingham and was an engineering teacher at Hoover High School from 2019 until 2021. In 2021, he joined the staff at the University of Michigan's Lurie Nanofabrication Facility.

Ruchi Sharma obtained B.Tech. in Electronics and Communication Engineering from NERIST, India, in the year 2005. She obtained M.Tech. in VLSI from Banasthali Vidyapith, India, in the year 2008, and Ph.D. in MEMS and Microelecorincs from IIT Delhi, India, in 2014. Between 2014 and 2017, she was a postdoctoral fellow at the University of Roma Tre, Rome, Italy, for a year and later joined the Department of Computer Science and Engineering, Washington University at Saint Louis, Missouri, USA, for a year. She joined the Biomedical Engineering Department at the University of Michigan as a postdoctoral research fellow in 2017. She was promoted to a Research Investigator in 2022. Dr. Sharma was awarded a distinction in the doctoral research and FITT award for best industry relevant Ph.D. thesis of 2014 at IIT Delhi. Her research includes MEMS and micro-electronics, microfabrication, electronics system design, gas sensors, portable gas chromatography, and its application in health care.

Anjali Devi Sivakumar received her B.Tech. in Electronics and Instrumentation Engineering from SASTRA Deemed to be University, India, in 2019. She obtained M.S. in Electrical Engineering and Computer Science, from the University of Michigan, in 2023, and is currently pursuing a Ph.D. in Electrical Engineering and Computer Science at the University of Michigan.

Chandrakalavathi Thota received B.S and M.S in Chemistry from Sri Venkateswara University in 2009 and 2011, India. She obtained Ph.D in chemistry from SRM Institute of Science and Technology, India, in the year 2021. She was a Postdoctoral fellow in Chungnam National University, South Korea from May 2021 to October 2021. Currently she is working as a Postdoctoral research fellow at University of Michigan.

Hongbo Zhu received B.S. from Xiamen University in 2012 and M.S. from the University of Nebraska – Lincoln in 2014, and Ph.D. from the University of Michigan in 2019.

Weishu Wu received his B.S. from Fudan University in 2018, and a M.Sc. from the University of Michigan in 2020. He is pursuing a Ph.D. in Biomedical Engineering at the University of Michigan.

Seong-Yong Jeong is an Assistant Professor in the Division of Advanced Materials Engineering at Kongju National University. He received a B.S. from Jeonbuk National University, South Korea, in 2015. He obtained his M.S. and Ph.D. integrated degrees from Korea University in 2021. He was a research professor at Korea University from 2021 to 2023. Between 2022 and 2023, he was a postdoctoral research fellow at the University of California, San Diego (USA) and later joined the Biomedical Engineering Department at the University of Michigan for half a year. His research interests include functional nanostructured materials, chemical sensors, and nanoelectronics.

Xudong Fan obtained B.S. and M.S. from Peking University in 1991 and 1994, and Ph.D. in physics and optics from Oregon Center for Optics atthe University of Oregon in 2000. Between 2000 and 2004, he was a project leader at 3 M Company. In August of 2004, he joined the Department of Biological Engineering at the University of Missouri as an assistant professor and was promoted to Associate Professor in 2009. In January of 2010, he joined the Biomedical Engineering Department at the University of Michigan and was promoted to Professor in 2014. Dr. Fan is a Fellow of Optical Society of America (now Optica), SPIE, and Royal Society of Chemistry (RSC). His research includes photonic bio/chemical sensors, micro/nano-fluidics, gas sensors, portable gas chromatography, and nanophotonics for disease diagnostics and bio/chemical molecule analysis.

Supplementary Material to

Microfluidic integration of μPID on μcolumn for ultracompact micro-gas chromatography

Xiaheng Huang[1,2,3,4,†], Shuo Yang[1,3,4,†], Wencheng Li[1,2,3,4], Robert Nidetz[5], Ruchi Sharma[1,3,4], Anjali Devi Sivakumar[1,2,3,4], Chandrakalavathi Thota[1,3,4], Hongbo Zhu[1], Weishu Wu[1,3,4], Seong-Yong Jeong[1,3,4], and Xudong Fan[1,3,4,*]

[1]Department of Biomedical Engineering,
University of Michigan, Ann Arbor, MI 48109, USA

[2]Department of Electrical Engineering and Computer Science,
University of Michigan, Ann Arbor, MI 48109, USA

[3]Center for Wireless Integrated MicroSensing and Systems (WIMS[2]),
University of Michigan, Ann Arbor, MI 48109, USA

[4]Max Harry Weil Institute for Critical Care Research and Innovation,
University of Michigan, Ann Arbor, MI 48109, USA

[5]Lurie Nanofabrication Facility,
University of Michigan, Ann Arbor, MI 48109, USA

*: Corresponding author: xsfan@umich.edu
†: Equal contribution

S1. Integrated µcolumn coating procedure

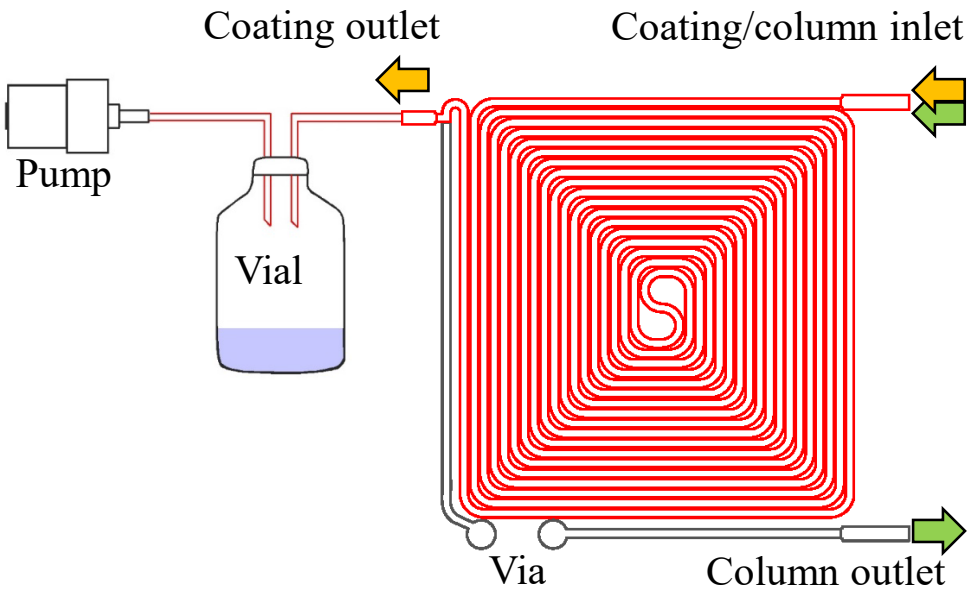

Figure S1. Coating procedure for integrated µcolumn on the iCPID. The coating solution (yellow arrows) was pulled by a voltage-controlled pump into the µcolumn inlet and routed into the coating outlet where it then flowed into an empty vial. The red-colored region indicates the channels that are coated. Note that the green arrows indicate the gas inlet and outlet during actual iCPID operation.

S2. Comparison between the integrated μPID on iCPID and the benchmark μPID

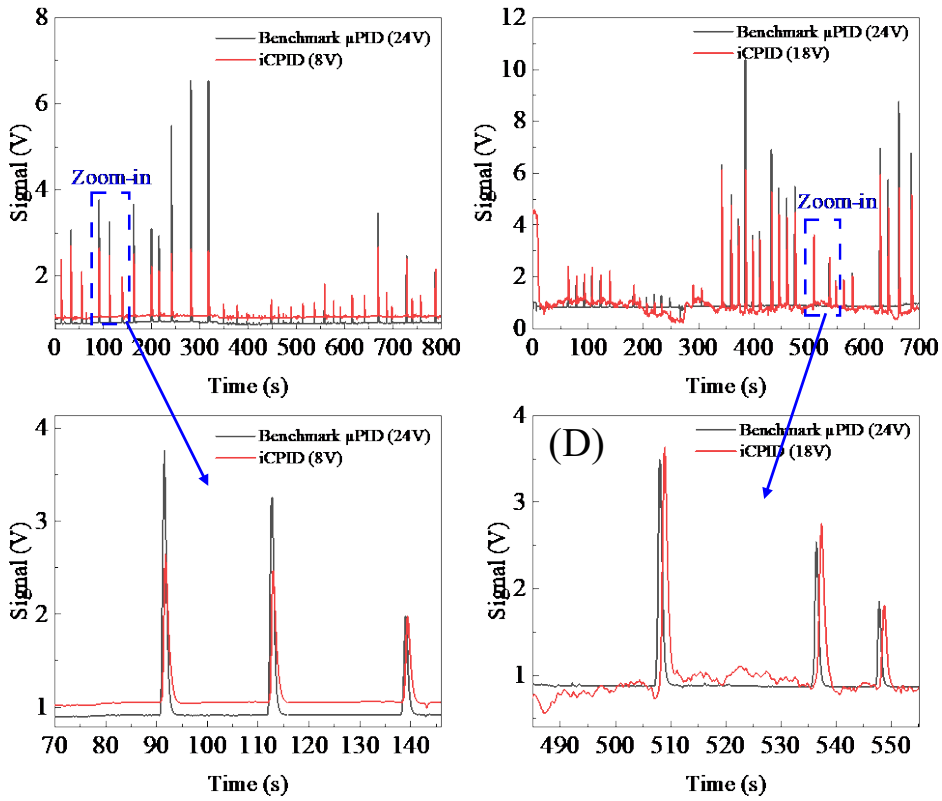

Figure S2. Chromatograms of the integrated μPID on the iCPID biased at (A) 8 V and (B) 18 V when connected in series with a benchmark μPID (biased at 24 V). (C) and (D) are zoom-in portions of (A) and (B). The chromatograms were generated by consecutive injections of different amounts of benzene using the setup shown in Figure 3(A) in the main text.

S3. Cause of the leaky buried oxide (BOX) in iCPID

This section discusses in detail the cause of the sublinear response of the integrated µPID. Figure S3(A) shows the simplified device structure of the benchmark µPID (or glass substrate based µPID), which consists of two conductive silicon electrodes forming a microfluidic channel on top of an insulating glass substrate. On the other hand, the integrated µPID (iCPID) adopts an SOI structure where the buried oxide (BOX) serves as an insulating layer to mimic the glass substrate of the benchmark µPID.

To investigate the cause of the distinctive features of the integrated µPID, we performed current-voltage measurement to compare its intrinsic electrical characteristics with those of the benchmark µPID. As shown in Figure S3, it was found that most integrated µPID exhibited a leakage current ranging from 10 nA to 100 µA at 20 V, whereas the benchmark µPID showed a constant current of 100 pA across a bias voltage from 0 to 20 V. Out of five devices constructed from two wafers, only one device (*i.e.*, iCPID D5) had an identical low and consistent current in I-V, enabling it to exhibit the same linearity as the benchmark µPID. The remaining four iCPIDs exhibited varying degrees of leaky I-V characteristics compared to the benchmark µPID. The benchmarking calibration curves presented in Figure 3 were measured using iCPID D1, which has a leaky current of up to 10 nA at 20 V and serves as a representative. The other leaky iCPIDs (*i.e.*, D2 to D4) also exhibited similar sublinear responses to concentrations.

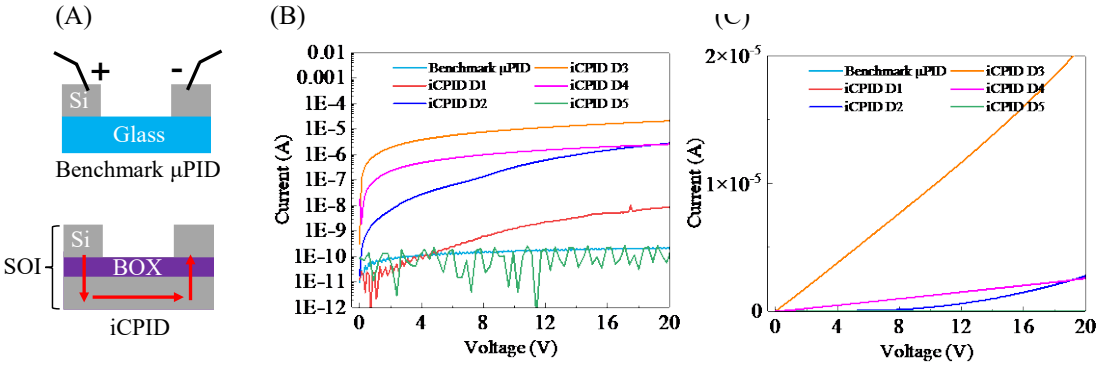

Figure S3. (A) Device structures of a benchmark µPID[2, 5] and an integrated µPID within the iCPID. (B) Semi-log scale and (C) Linear-linear scale of current-voltage (I-V) characteristics of a benchmark µPID, and five different iCPIDs. All devices were packaged microfluidically and electrically.

To investigate the possible role of BOX in the aforementioned electrical leakage. We fabricated a stand-alone SOI µPID (without µcolumn integration to eliminate any impact from the additional process steps). The microfabrication process (see Figure S4) was identical to a benchmark µPID. The only difference was the substitution of the glass substrate for an oxidized silicon wafer, which was bonded using fusion bonding. Figure S5 presents the I-V characteristics and sensing performance of a stand-alone SOI µPID. Similar to most of the leaky iCPIDs, this stand-alone SOI µPID had a high leakage current of up to 100 µA at 20 V, resulting in 5-fold reduction in sensitivity and bias voltage dependent sublinear responses. These results suggest that the BOX within the SOI based µPID structure experienced leakage after fabrication, which caused sensitivity reduction and sublinear response.

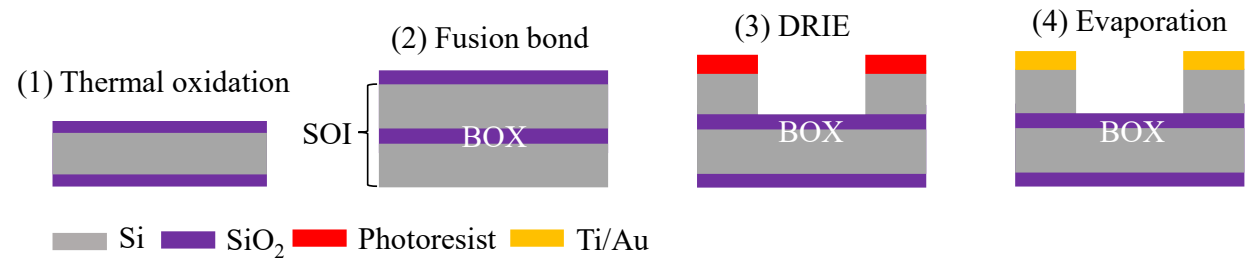

Figure S4. Microfabrication process of stand-alone SOI µPIDs. (1) Thermal oxide is grown on a Si wafer. (2) An SOI wafer is created by fusion bonding the oxidized wafer to a highly doped Si wafer. The conductive wafer serves as the device layer and the oxidized wafer serves as the handle layer. (3) Patterned photoresist is used as a mask for the DRIE on the device layer to generate the µPID. The µPID was etched down to the BOX. (4) Ti/Au is evaporated on the silicon electrodes using a Kapton tape covering the center microfluidic channels as patterning.

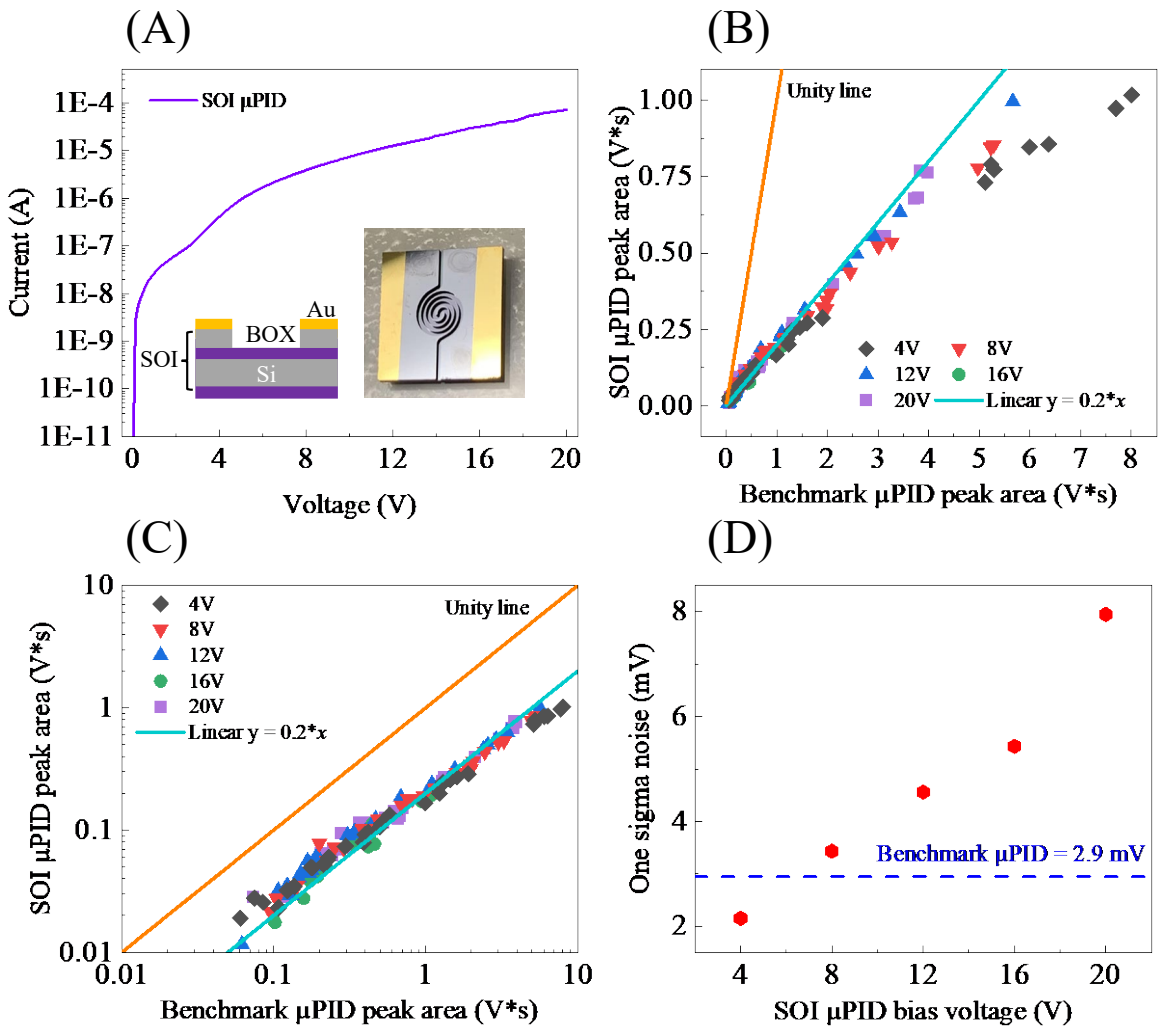

Figure S5. (A) Current-voltage (I-V) characteristics of an SOI µPID. Inset shows the device structure and a photograph of the SOI µPID. (B) SOI µPID peak area (biased from 4 to 20 V) vs. benchmark µPID peak area (constantly biased at 24 V).

To further reveal the formation of the leaky BOX, metal-oxide-semiconductor (MOS) structures were fabricated to assess the electrical performance of BOX before and after fusion bonding. Figure S6(A) shows that the thermal oxide layer was intrinsically insulating regardless of its thickness with a flat current of several pA across the bias voltage up to 24 V. In comparison, as shown in Figure S6(B), the post-fusion bonding structure demonstrated a leaky performance indicating that the BOX layer became leaky after the fusion bonding process[6]. A smaller area sample also gives the leakage feature with an decreased current. This suggests that the presumably post-fusion bonding defect sites are not localized but universally existent across the BOX layer.

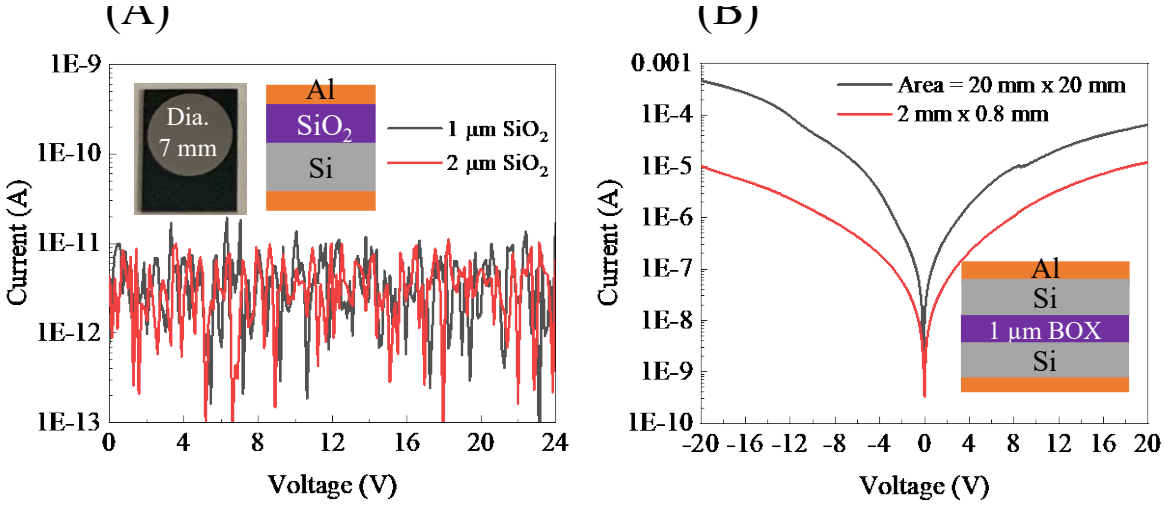

Figure S6. Current-voltage (I-V) characteristics of (A) a metal-oxide-semiconductor (MOS) structure comprising Al/SiO_2/Si/Al with a device diameter = 7 mm. The thicknesses of thermal SiO_2 tested are 1 µm and 2 µm, respectively. Inset shows the structure and a photograph of the device. (B) Post-fusion bonding MOS structure comprising Al/Si/SiO_2(BOX)/Si/Al with 1 µm of BOX. The sample areas were 20 mm x 20 mm and 2 mm x 0.8 mm. The top and bottom Al contacts were probed in these two structures.

To explore potential solutions to this issue, several strategies were explored. First, the fusion bonding was performed at an elevated temperature of 1100 ºC which presumably would result in a better bond. However, the BOX still exhibited leakage. Second, the thickness of the BOX layer was increased from 2 µm to 4 µm fusion bonding two oxidized Si wafers with a 2 µm thermal oxide layer on each. As shown in Figures S7(A)-(C), all devices demonstrated varying degrees of leaky performance similar to iCPIDs. Lastly, a commercial SOI wafer (device layer: <100>, p-type, 0.001-0.005 Ω*cm, 50 µm thick; BOX = 2 µm; handle wafer: <100>, p-type, 1-10 Ω*cm, 500 µm thick; Ultrasil LLC) was also tested, but similar results were observed (Figure S7(D)).

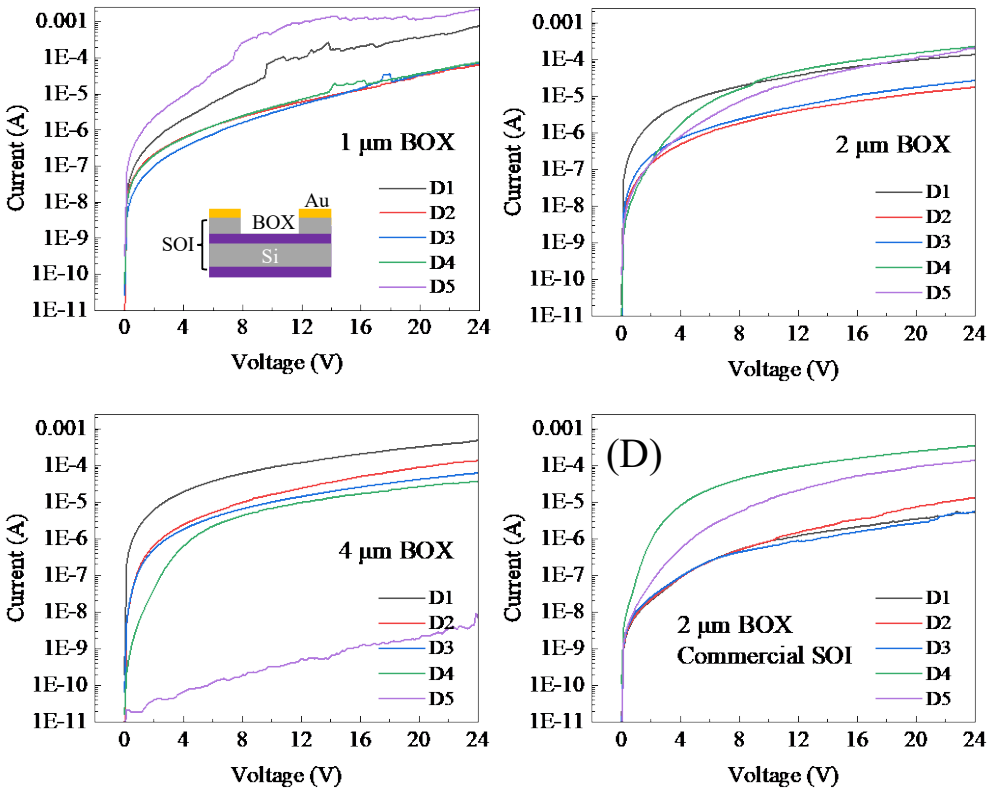

Figure S7. Current-voltage (I-V) characteristics of an SOI µPID comprising a BOX with a thickness of (A) 1 µm (B) 2 µm (C) 4 µm and (D) using a BOX = 2 µm commercial SOI wafer. Five devices out of 36 were measured from each wafer. Fusion bonding was performed at 1100 ºC for 2 hours in furnaces for this batch of wafers in (A)-(C).

S4. Thermal modeling

We simulated heat transfer in an integrated device to obtain the temperature profile on the chip using COMSOL Multiphysics®. The results are shown in the inset of Figure 4(A). The Heat Transfer in Solids module was used in the simulation, and we considered only conduction heat transfer physics with an assumption that the other types of heat loss (convection and radiation) in the device is minimal. The geometry used in the simulation was a simplified version of the actual device structure, with an in-plane layout identical to the real device. A 0.8 mm thick silicon layer was stacked on top of a 0.5 mm thick borosilicate glass layer in the out-of-plane direction. The heat source was a patterned platinum heater (0.3 mm thick in the simulation, for simplicity) set to a temperature of 100 ^{o}C. The entire geometry was surrounded with an air cube (shown in the inset of Figure 4(A)) maintained at a constant temperature of 25 ^{o}C to provide a boundary condition and emulate the ambient environment operation of the device.

S5. Integrated μcolumn separation efficiency evaluation

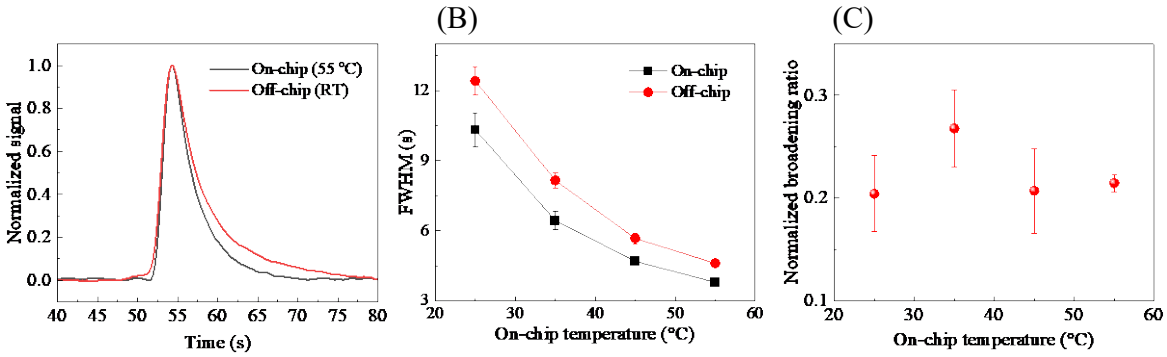

Figure S8. (A) Chromatograms of the test analyte, chlorobenzene, generated using on-chip and off-chip μPID with the iCPID ramped to 55 °C. Filtered air was used as the carrier gas with a flow rate of ~0.8 mL/min. (B) Full-width-at-half-maximum (FWHM) of chlorobenzene from room temperature to 55 °C. (C) Normalized broadening ratio = ($FHWM_{off\text{-}chip}$ - $FHWM_{on\text{-}chip}$)/$FHWM_{on\text{-}chip}$ vs. on-chip temperature. Error bars were obtained from five measurements.

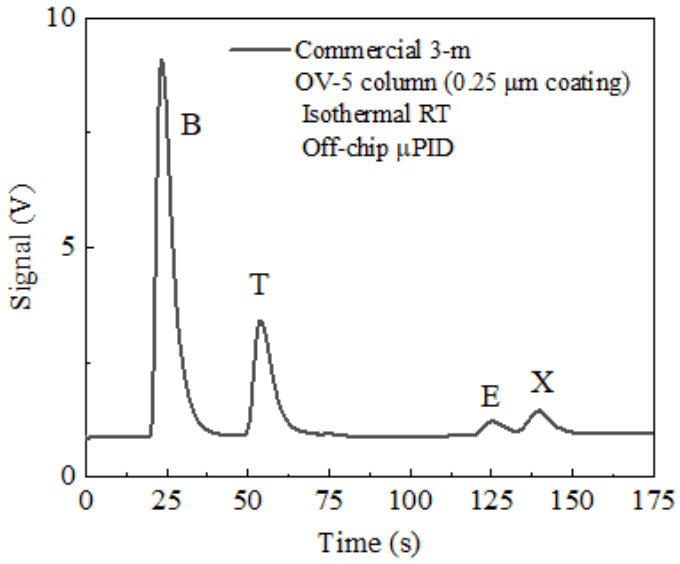

Figure S9. A chromatogram of BTEX generated using a commercial 3-m OV-5 column (0.25 μm coating thickness, #122-5562, Agilent Technologies) with the off-chip stand-alone μPID. The column was operated isothermally at room temperature. Helium was used as the carrier gas with a flow rate of 1 mL/min. The chromatographic results are listed in Table S3.

S6. Ultracompact system - components fabrication and assembly

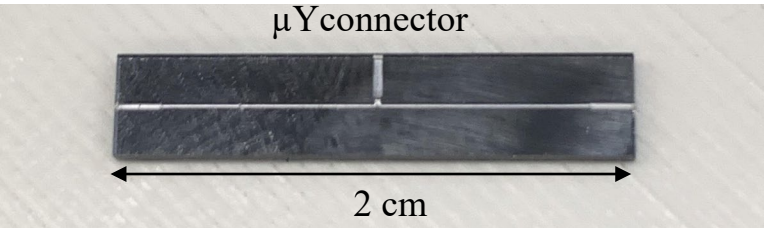

Figure S10. Photograph of a µYconnector (µYconn.) used in the system. The microfabrication process is reported in previous work[7].

Preparation and operation of preconcentrator

The stainless-steel preconcentrator was fabricated the same way reported before[7].

Air filter preparation

Ambient air was pumped by a pump from Artshu (#244127942) to flow through a hydrocarbon-moisture filter to generate clean and dry air to be used as a carrier gas. To build the filter, a 0.25-inch-diameter, 2-inch-long stainless steel (SS) tube from McMaster (#1443N134) was first deactivated by Silcotek Corporation. Next, we prepared a four-bed hydrocarbon-moisture filter. The first bed was silica gel beads (#FD-filter-molecular from Forensics Detectors) for trapping moisture. The second bed was a 4-angstrom pore opening molecular sieve 5A from Forensics Detectors. The third bed was a smaller granule size molecular sieve 5A, 60-80 mesh (#20302, Sigma Aldrich). The final bed was activated charcoal (#05112-100G, Sigma Aldrich). Both tube ends were closed and sealed using glass wool. The filter was preconditioned at 150 °C for 12 h under helium flow before use.

3D printing box procedure

The enclosure for the iCube with dimensions 108 mm x 94 mm x 85 mm (length x width x height) was designed using Autodesk Fusion 360 and 3D printed using Ultimaker S5 3D printer with PLA (Ultimaker) as the 3D printing material.

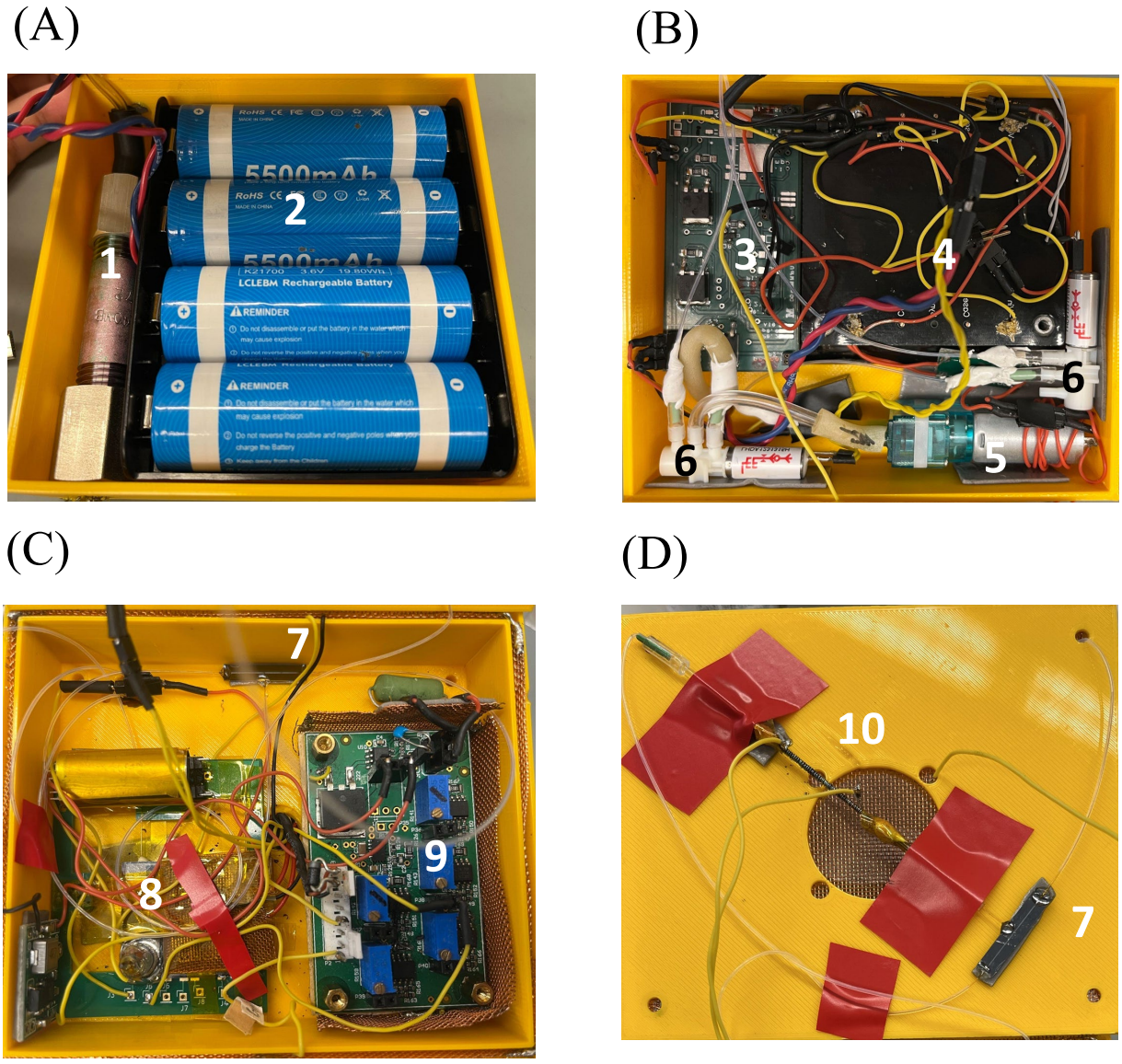

Figure S11. (A)-(C) First, second, and third layer of the iCube. (D) Top lid. (1) Filter. (2) Battery pack (a set of four 5500 mAh rechargeable battery). (3) Printed circuit board and data acquisition card (NI DAQ). (4) DC-DC converter. (5) Pump. (6) 3-port valves. (7) µYconnector (see Figure S5). (8) Packaged iCPID (a small DC-DC converter for bias-voltage tuning on the sidewall). (9) Amplification and plasma excitation circuit for µPID. (10) Preconcentrator.

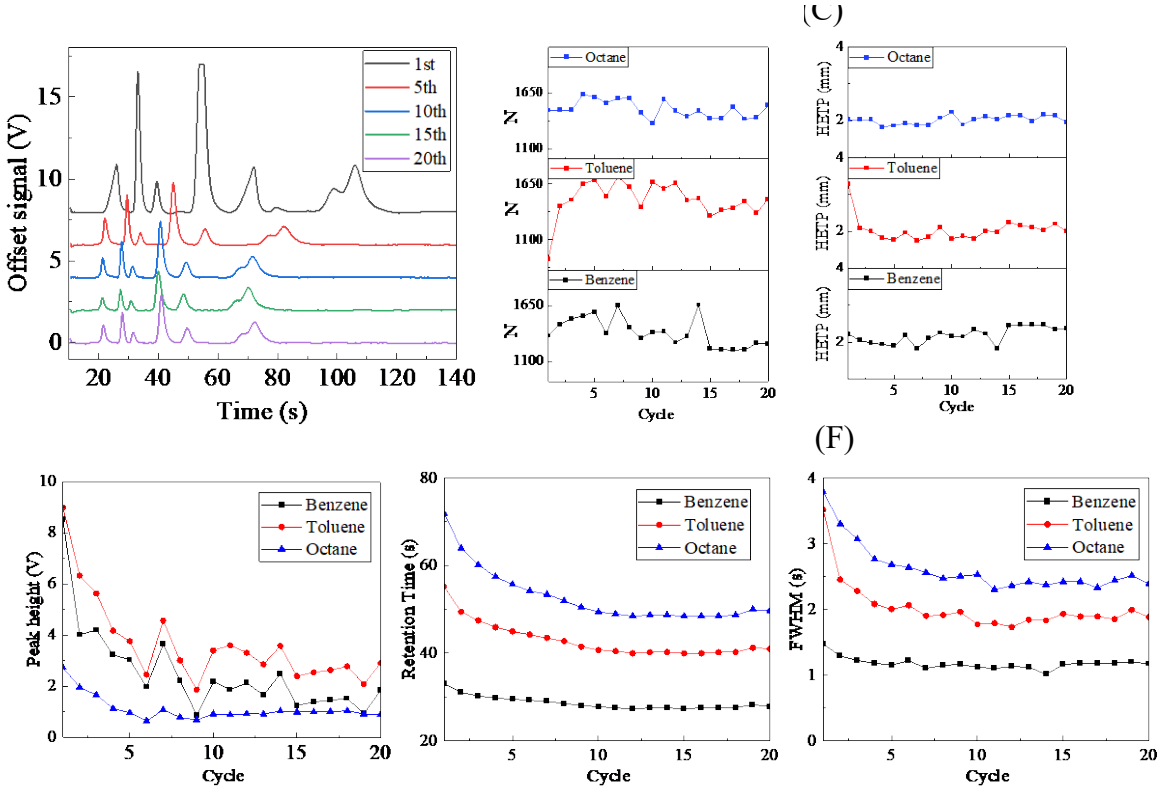

Figure S12. (A) 1st, 5th, 10th ,15th, and 20th chromatograms generated by iCube with the same mixture of chemicals sampled with the same amount each time and analyzed under identical conditions. Each analysis run was followed by a clean run. The flow rate was ~0.84 mL/min. (B) Number of theoretical plate (N). (C) Height equivalents to theoretical plates (HETPs). (D) Peak height; (E) Retention time; and (F) Full-width-at-half-maximum (FWHMs) for benzene, toluene, and octane, which are included in this mixture.

#	Analyte	Boiling point (°C)	Concentration in bag (mg/L)
1	Acetone	56.2	0.21
2	Benzene	80.1	0.29
3	Heptane	98	0.27
4	Toluene	110.6	0.29
5	Octane	125.6	0.23
6	Butyl acetate	126.1	0.29
7	Ethylbenzene	136	0.29
8	Xylene	138.3	0.29

Table S1. VOC list of test compounds and the corresponding concentrations in the bag. The sampling time was 3 s at a sampling rate of 8 mL/min.

Item	P/N	Company
Norland optical adhesive 68T	68T01	Norland
Hysol 1C Epoxy	1373425	Ellsworth Adhesive
Deactivated fused silica tubing	10010	Restek
PTFE Tubing	06417-11	Cole-Parmer
Latex tubing	ZUSA-HT-227	Motion Industries
Zeus PTFE Extruded Regular Wall Tubing	SWTT-14-C	Component Supply
32-gauge nickel chromium wire	32BNC	Consolidated
Krypton lamp for PID	043-257	MOCON baseline
PCB board	Not applicable	M.A.K.S.
3-port valve	LHDA1231315H	Lee Company
Pump	244127942	Artshu
Transformer for PID excitation	CCFL FL3209	Coil Craft
DC to DC convertor	TEP 160-2415WIR	Digikey
Copper mesh	B08PT35XRD	Amazon
Battery	B098QFZW1V	Amazon

Table S2. Materials for the system assembly.

Commercial column + off-chip μPID detection	RT (s)	FWHM (s)	N	HETP (mm)
Benzene	23.0	5.9	84.8	35.4
Toluene	53.6	6.3	406.4	7.4
Ethylbenzene	125.4	8.0	1356.3	2.2
p-Xylene	139.7	8.0	1686.7	1.8
iCPID with on-chip μPID detection				
Benzene	23.3	1.9	867.4	3.5
Toluene	38.6	2.9	997.1	3.0
Ethylbenzene	75.9	5.3	1155.5	2.6
p-Xylene	96.9	6.5	1230.4	2.4
iCPID with off-chip μPID detection				
Benzene	25.1	2.6	503.6	6.0
Toluene	40.6	3.5	742.9	4.0
Ethylbenzene	78.4	6.3	871.3	3.4
p-Xylene	99.7	7.0	1120.5	2.7

Table S3. Retention times (RTs), full-widths-at-half-maximum (FWHMs), number of theoretical plate (N), and height equivalents to theoretical plates (HETPs) of the 3-m OV-5 commercial column using the off-chip μPID, and the 3-m OV-5 integrated μcolumn using both on-chip and off-chip μPIDs, respectively. All columns were operated at room temperature.

Operation	Component	Operation time	Energy	Comment
Sampling	Pump	3 s	4.05 J	Sampling Mode 1 Continuous sampling @1.35 W (3 V x 0.45 A)
Analyzing	Pump (carrier gas)	6 min = 360 s	480 J	@1.35 W (3 V x 0.45 A)
	Pre-concentrator	5.4 s	~2,000 J	Based on actual measurement
	PID	6 min = 360 s	45 J (@ 0.125 W)	Based on actual measurement
Total energy: 2.53 kJ				
Power supply	Battery	-	285 kJ	Battery voltage = 3.6 V Battery current = 5.5 A*H 4 batteries
Total working cycles = 110 Total working time = 11 h				

Table S4. iCube power consumption, and the total working cycles and time.

References

1. Zhu, H.; Nidetz, R.; Zhou, M.; Lee, J.; Buggaveeti, S.; Kurabayashi, K.; Fan, X., Flow-through microfluidic photoionization detectors for rapid and highly sensitive vapor detection. *Lab on a Chip* **2015,** *15* (14), 3021-3029.
2. Li, M. W.-H.; Ghosh, A.; Venkatasubramanian, A.; Sharma, R.; Huang, X.; Fan, X., High-Sensitivity Micro-Gas Chromatograph−Photoionization Detector for Trace Vapor Detection. *ACS Sens.* **2021,** *6*, 2348-2355.
3. Greening, J., Saturation characteristics of parallel-plate ionization chambers. *Physics in Medicine & Biology* **1964,** *9* (2), 143.
4. Mie, G., Der elektrische Strom in ionisierter Luft in einem ebenen Kondensator. *Annalen der Physik* **1904,** *318* (5), 857-889.
5. Zhu, H.; Nidetz, R.; Zhou, M.; Lee, J.; Buggaveeti, S.; Kurabayashi, K.; Fan, X., Flow-through microfluidic photoionization detectors for rapid and highly sensitive vapor detection. *Lab Chip* **2015,** *15* (14), 3021-9.
6. Afanas' ev, V.; Ericsson, P.; Bengtsson, S.; Andersson, M. O., Wafer bonding induced degradation of thermal silicon dioxide layers on silicon. *Applied physics letters* **1995,** *66* (13), 1653-1655.
7. Huang, X.; Li, M. W.-h.; Zang, W.; Huang, X.; Sivakumar, A. D.; Sharma, R.; Fan, X., Portable comprehensive two-dimensional micro-gas chromatography using an integrated flow-restricted pneumatic modulator. *Microsystems & Nanoengineering* **2022,** *8* (1), 115.